Ore Geology Reviews 138 (2021) 104408

Contents lists available at ScienceDirect

Ore Geology Reviews

journal homepage: www.elsevier.com/locate/oregeorev

Genesis and fluid evolution of the Huangtan Au-Cu deposit in the Kalatag district, Eastern Tianshan, NW China: Constraints from geology, geochronology, fluid inclusions, and H-O-S-Pb isotope geochemistry

Bingke Sun [a], Banxiao Ruan [b,*], Xinbiao Lv [a,b], Zhihui Dai [c], Chen Mao [a]

[a] Faculty of Earth Resources, China University of Geosciences, Wuhan 430074, China
[b] Institute of Geological Survey, China University of Geosciences, Wuhan 430074, China
[c] State Key Laboratory of Deposit Geochemistry, Institute of Geochemistry, Chinese Academy of Sciences, Guiyang 550081, China

ARTICLE INFO

Keywords:
Huangtan deposit
Fluid inclusions
Stable isotopes
Ar-Ar geochronology
VMS-type Au-Cu mineralization
Eastern Tianshan

ABSTRACT

The newly discovered Huangtan Au-Cu deposit is located in the central Dananhu - Tousuquan arc of Eastern Tianshan, southern Central Asian Orogenic Belt (CAOB). It is the first Au-dominated volcanogenic massive sulfide (VMS) polymetallic deposit in the Eastern Tianshan. Veinlet-disseminated and massive orebodies are hosted within Early Silurian pyritic phyllic tuff and volcanic breccia and controlled by a secondary fracture zone of the Kalatag fault with extensive hydrothermal alteration. Four primary alteration/mineralization stages have been recognized as follows: (1) Early ore stage (S1), forming mainly ore-barren fine quartz veins with minor gold-bearing sulfides; (2) main ore stage (S2), forming mainly thick quartz veins with abundant coarse-grained subhedral pyrite (S2-1), and plentiful chalcopyrite, sphalerite, barite and Au-bearing sulfide veins (S2-2); (3) late ore stage (S3), which is characterized by plenty of barren quartz–calcite veins with few sulfides; and (4) supergene stage (S4), accompanied by abundant oxide mineralization, including malachite, jarosite and other supergene minerals. From S1 to S3, microthermometric data of fluid inclusions show homogenization temperatures of 263–379 °C (mean = 308 °C), 188-292 °C (mean = 240 °C), and 118-198 °C (mean = 158 °C), respectively, and salinities of 5.3–14.2 (mean = 10.8) wt.% NaCl equiv., 2.8–10.7 (mean = 7.6) wt.% NaCl equiv., and 0.3–14.1 (mean = 2.6) wt.% NaCl equiv., respectively. The ore-forming fluids are characterized by middle-low temperature, low salinity, relatively reduced condition, and an H_2O-NaCl ± CO_2 ± CH_4 system.

The $\delta^{34}S$ values (−5.25‰ to 0.50‰) and Pb isotopic ratios ($^{206}Pb/^{204}Pb$ = 17.868–19.495, $^{207}Pb/^{204}Pb$ = 15.446–15.575, and $^{208}Pb/^{204}Pb$ = 37.350–38.491) suggest that the ore-forming materials came predominantly from a deep-seated magma source with a minor contribution of lower continental crust. The $\delta^{18}O_{H2O}$ and $\delta D_{V\text{-}SMOW}$ values of fluid inclusions in each metallogenic stage range from −6.1 to 5.6‰ and −66.8 to −53.9‰, respectively, suggesting the dominant role of magmatic water mixed with convectively circulating heated seawater during fluid evolution. Fluid cooling dilution, local boiling, and fluid mixing were considered as the main mechanisms of metal precipitation. The $^{40}Ar\text{-}^{39}Ar$ plateau age of hydrothermal muscovite from the late ore stage (S3) is 414.4 ± 0.4 Ma, which represents the upper limit age of shallow hydrothermal alteration and Au-Cu mineralization. It is also consistent with the Early Silurian polymetallic metallogenic event in the Kalatag district. The auriferous Huangtan and adjacent Cu-Zn-rich Huangtupo VMS deposits show obvious ore-forming element differences, and constitute a unique VMS metallogenic system in the Eastern Tianshan Orogenic Belt (ETOB), which provides an important research object and new insight for ore prospecting in the peripheral Gobi Desert area.

1. Introduction

Volcanogenic massive sulfide (VMS) deposits, also known as volcanic-hosted massive sulfide (VHMS), are important sources of Cu, Zn, Pb, Au, and Ag in a metal-dependent global economy (Poulsen and Hannington, 1996; Huston, 2000; Franklin et al., 2005; Dubé et al.,

* Corresponding author at: China University of Geosciences, 388 Lumo Road, Hongshan District, Wuhan, China.
E-mail address: bxruan@foxmail.com (B. Ruan).

https://doi.org/10.1016/j.oregeorev.2021.104408
Received 27 February 2021; Received in revised form 6 August 2021; Accepted 8 August 2021
Available online 14 August 2021

2007; Mercier-Langevin et al., 2011; Hokka, 2020). Generally, VMS deposits occur in a variety of tectonic settings but are typically related to precipitation of metals from hydrothermal fluids circulating in volcanically active submarine environments (Ohmoto et al., 1983). These hydrothermal fluids are composed of a variable mixture of magmatic-hydrothermal fluids and evolved seawater that has reacted with underlying rocks, with most systems dominated by evolved seawater (Franklin et al., 1981). Characterizing sources of metallogenic materials and fluids is the key to understanding metallogenic evolution in hydrothermal systems. Fluid inclusions trapped in hydrothermal minerals record much information of the primary ore-forming fluids during the geological history and can provide crucial samples to reestablish the physicochemical conditions of paleomineralization of ancient hydrothermal deposits (Franklin et al., 2005). As we all know, the active seafloor geothermal systems can provide important clues to the origins of polymetallic hydrothermal ore deposits. However, the ancient VMS deposits are more important targets for mineral exploration, and the study of their metallogenic mechanism can help us understand the interrelationships between metal endowment and the hydrothermal altered, accretionary, preservational, weathered, and depositional systems. This is conducive to the further development of mineral resources (Hannington et al., 2005; de Ronde et al., 2011; Pilote et al., 2020).

Situated at the northern part of the ETOB, the Kalatag district forms part of the E-W trending Dananhu-Tousuquan island belt, which extends along the southern margin of the Turpan-Hami basin (Fig. 1). Based on an extensive field investigation and precise geochronological data, Zhang et al., (2008) proposed that the polymetallic mineralization in the ETOB can be divided into four stages: (1) a subduction-related island arc stage during 360–320 Ma, represented by the Tuwu-Yandong porphyry Cu deposits (Liu et al., 2003); (2) a collisional-accretionary stage (300–280 Ma), exemplified by Kanggur gold deposit (Zhang et al., 2003); (3) a post-collisional-extension stage (280–270 Ma) with mafic–ultramafic Cu-Ni deposits, such as the Huangshandong deposit (Mao et al., 2015a; Mao et al., 2015b); and (4) an intracontinental extensional stage (240–220 Ma), typically represented by the giant Donggebi Mo deposit (Wu et al., 2014). However, increasing Ordovician-Silurian arc magmatism and mineralization have been reported in the northern part of ETOB in the recent decade, indicating the Early Paleozoic is an important episode for Cu-polymetallic mineralization (Mao et al., 2015a; Mao et al., 2015b; Xiao et al., 2015; Wang and Zhang, 2016; Sun et al., 2020).

The newly discovered Huangtan Au-Cu deposit is the first gold-dominated polymetallic deposit in the Kalatag district, and it provides a new studying object for the Early Paleozoic Cu-polymetallic mineralization in ETOB (Fig. 2). It has a currently cumulative estimated resource of Au (5 t@ > 1g/t), Cu (10Kt@0.3%), and Zn (100Kt@1.5%) (Deng et al., 2020), and only minimal basic geological research has been undertaken. Liang (2018) conducted a preliminary ore deposit geology and genesis study and considered the deposit as a subvolcanic hydrothermal Au-Cu polymetallic deposit controlled by tectonics. However, He (2019) and Sun et al. (2020) considered that it was another VMS-type deposit associated with the adjacent Huangtupo VMS deposit (Fig. 2). The unique spatiotemporal relationships between the two deposits provide an excellent opportunity to investigate the Early Paleozoic VMS

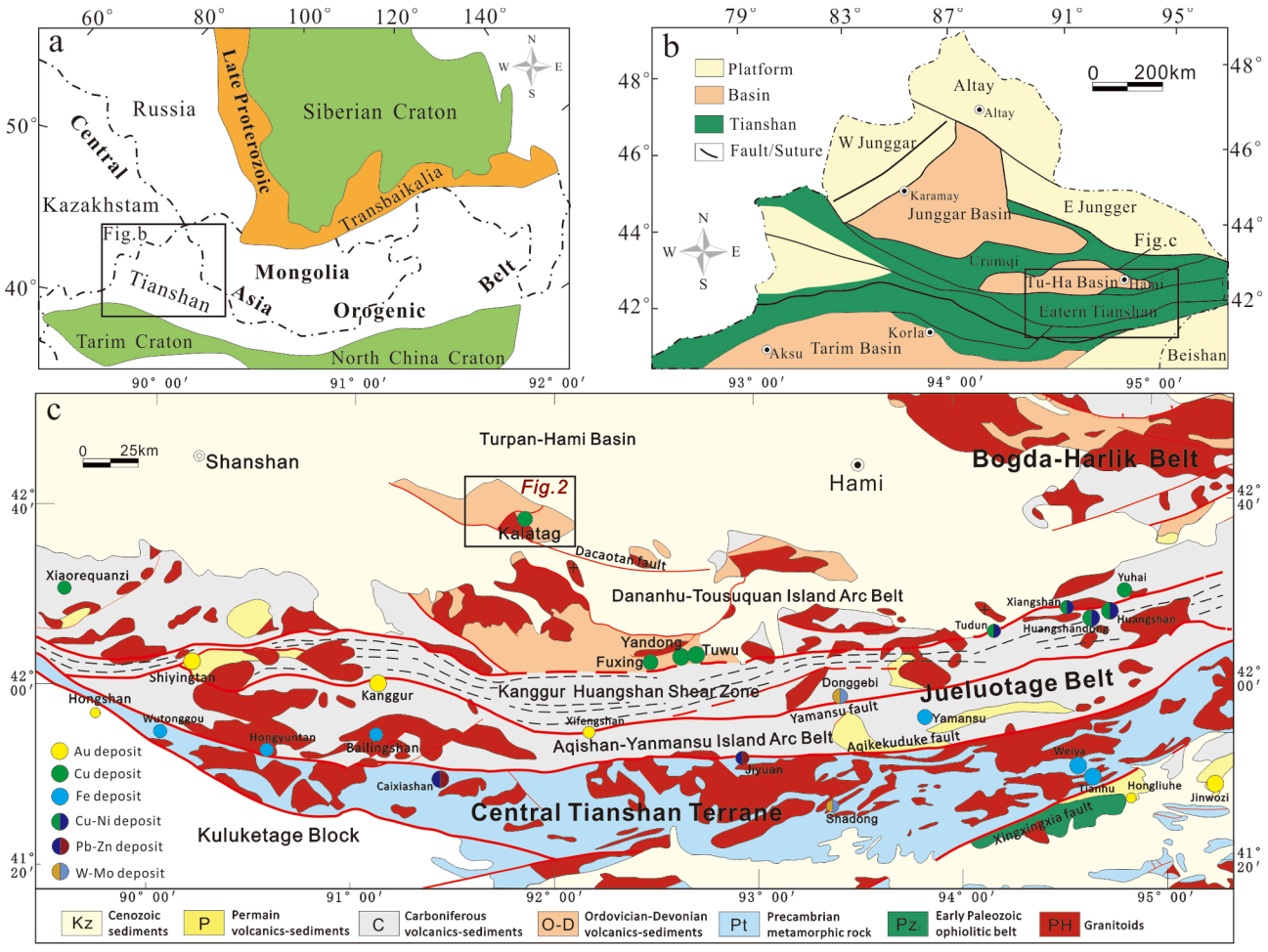

Fig.1. a: Location of the study area in the Central Asia Orogenic Belt (modified from Şengör et al., 1993); b: Sketch map showing the geological units of the Tianshan Belt (modified from Chen et al., 2012); c: Simplified geological map of the Eastern Tianshan Belt (modified from Wang et al., 2006).

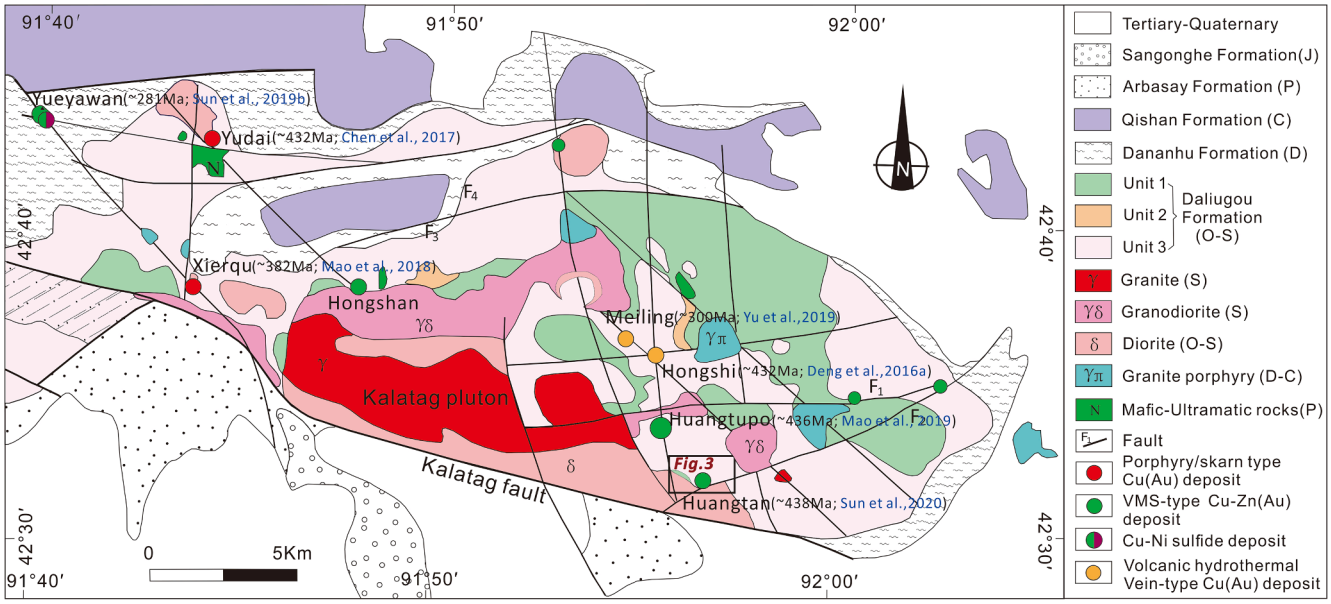

Fig. 2. Geological sketch map of the Kalatag district (modified from Mao et al., 2019. Chronological data from Deng et al., 2016a; Chen et al., 2017; Mao et al., 2018, 2019; Yu et al., 2019; Sun et al., 2019b; Sun et al., 2020).

mineralization system in the ETOB. Thus far, the ore-forming fluids, metallogenic materials, and metallogenic processes of the Huangtan deposit remain unclear. In this study, we conducted a comprehensive investigation of the geological and mineralization characteristics, fluid inclusions (petrography, Laser Raman, and microthermometry), S-Pb-H-O isotopes geochemistry, and mineralization epoch (muscovite Ar-Ar) to constrain the origin and evolution of the hydrothermal system. Finally, a comprehensive metallogenic model was proposed to explain the Early Paleozoic VMS mineralization in the Kalatag district after comparison with the adjacent Huangtupo VMS deposit. This dataset would provide new insights on the prospectivity for VMS Cu-polymetallic mineralization in southern CAOB.

2. Geological setting

The CAOB, which sandwiched between the European and Siberian cratons in the north and the Tarim and North China cratons in the south (Fig. 1a; Şengör et al., 1993; Windley et al., 2007; Pirajno, 2013; Xiao et al., 2013; Xiao et al., 2015), is formed by multiple subduction-accretion of island arcs, oceanic plateau, seamounts, ophiolites and microcontinents that occurred from the Late Proterozoic to the Mesozoic (Goldfarb et al., 2001, 2014; Li et al., 2013).

The ETOB has been considered as a part of the southern margin of the CAOB and is located between the Junggar basin in the north and the Tarim basin in the south (Fig. 1b; Goldfarb et al., 2001, 2014; Zhang et al., 2017). Multistage intensive magmatic-hydrothermal-tectonic events had led to the formation of many giant hydrothermal and magmatic deposits. It can be divided into three major tectonic zones: the Central Tianshan Terrane, the Jueluotage belt, and the Bogda–Harlik belt from the south to the north with different rock assemblages and distinctive mineralization (Fig. 1c; Pirajno et al., 2011).

The Jueluotage Belt is characterized by middle Paleozoic volcanic and sedimentary strata. This belt can be further subdivided into three tectonic subunits by the E-trending regional-scale Aqikuduke, Kanggur, Yamansu, and Dacaotan faults, including the Aqishan-Yamansu island arc belt, the Kanggur-Huangshan ductile shear zone, and the Dananhu-Tousuquan island arc belt from south to north (Fig. 1c; Huang et al., 2013; Wang and Zhang, 2018). The Dananhu-Tousuquan island arc belt is located in the north of the ETOB, between the Turpan-Hami Basin and the late Carboniferous Kanggur suture zone (Xiao et al., 2004). This belt has been considered as an Ordovician to Carboniferous island arc accompanied by a set of marine calc-alkaline mafic-felsic lavas, tuffs, volcaniclastics, and flysch sediments, which were generally subjected to weak metamorphism of low greenschist facies from Ordovician to Early Silurian (Xiao et al., 2004; Mao et al., 2015a). A series of economically significant Paleozoic Cu-Zn-Au-Ni deposits developed in this belt, such as the Silurian Kalatag Cu deposits, the Carboniferous Tuwu-Yandong porphyry Cu deposits, and the Permian Huangshan - Huangshandong Cu-Ni deposits (Shen et al., 2014).

The Kalatag district consists of a NW-trending Paleozoic anticline in the north part of the Dananhu-Tousuquan island arc belt (Mao et al., 2019). The EW-trending Kabei fault and the NWW-trending Kalatag fault represent the northern and southern boundaries, respectively. The strata in this region predominantly comprise of Paleozoic mafic to felsic volcanic, volcaniclastic, and sedimentary rocks intruded by Ordovician to Permian granitic intrusions, which belong to the Daliugou (O-S), Hongliuxia (S) formations (Fig. 2). In addition, these rocks are unconformably overlain and surrounded by volcanic-sedimentary rocks that belong to the Dananhu (D), Qishan (C), and Arbasay (P) formations outwards from the Kalatag anticlinal hinge (Fig. 2). The Ordovician-Silurian Daliugou Formation (O_d), which is the most important ore-bearing stratum, contains three sequences from bottom to top: Unit 1 is composed of deep marine basalts, basaltic andesites, andesites, and volcaniclastic rocks; Unit 2 is dominated by strongly altered tuff, tuffaceous breccia, and pyroclastic dacite, with minor siliceous rocks and rhyolite intercalation, and Unit 3 consists chiefly of breccia, rhyolites and dacitic lava with minor interbedded tuffs (Fig. 2; Mao et al., 2019; Deng et al., 2020). Seven Cu–polymetallic deposits, including VMS-type Cu-Zn(Au) deposit (e.g., Huangtupo, Huangtan); hydrothermal vein-type Cu(Au) deposits (e.g., Hongshi, Meiling, Hongshan); porphyry-type Cu deposit (e.g., Yudai); skarn-type Fe-Cu deposit (e.g., Xierqu) and Ni-Cu sulfide deposits (e.g., Yueyawan), were discovered either in the Early Paleozoic or the early Late Paleozoic rocks in the northwestern part of the Kalatag district (Sun et al., 2019a; Deng et al., 2020).

3. Ore deposit geology

The Huangtan deposit is located on the southern edge of the Kalatag district (Fig. 2). The main lithostratigraphic units of this deposit are the Daliugou Formation, which is composed of the lower intermediate-acid

volcaniclastic rock interlayered with basaltic andesite and andesite (Unit 1) and the upper intermediate-acid volcanic rocks intercalated with tuff (Unit 2–3). The quartz diorite crops out in the southwest part of the ore district and concordantly intruded into the Daliugou Formation. The later pyritic phyllic rhyolite porphyry occurs as dyke and is locally distributed in the central and northeastern part of the Huangtan area (Fig. 3).

Polymetallic mineralization occurred mainly within the central part of the alteration zone of beresitization near the contact zone of the tuff and lower breccia (Fig. 4a, b). The Au-Cu polymetallic ore bodies are primarily distributed in the altered fracture zone controlled by the NW-, EW- and NNE-trending faults and all buried below 30 m from the surface. They are mainly characterized by gold-bearing sulfide-quartz veins. The Cu-Zn orebodies of the Huangtan are mainly stratiform and lenticular in the slope zone at the periphery of the volcanic structure. Surrounding rock alteration is characterized by beresitization, with relatively weak alteration in the upper tuff of the orebody (Fig. 5a, c). As the second-order tectonic-alteration belt of the Kalatag fault, the NW-trending faults are the most important ore-controlling and ore-hosting structures (Fig. 3). The geophysical anomalies are marked by low resistance and high polarization, which are similar to the neighboring Huangtupo VMS deposit, indicating that it experienced early Paleozoic submarine volcanic exhalative hydrothermal-sedimentary mineralization (Deng et al., 2018). Thus far, several orebodies (3 Au, 1 Zn, 1 Au-Cu-Zn, and 1 Zn orebodies) have been found around the Huangtan deposit (Liang, 2018). The main gold orebodies controlled by strongly pyritic phyllic wall rocks are of veins and branches with the average grade 2.81 g/t and have a length and thickness of 125 m and 1.67–17.97 m, respectively. The major Au-Cu-Zn ore body (Fig. 5c) associated with the Au ore body has an average length of 230 m, a thickness of 3.28–20.55 m, and with an ore grade of Cu > 0.75 wt%, Zn > 0.85 wt%, Au > 1.15 g/t, and Ag > 20.65 g/t. The metallogenic elements such as copper, gold and silver showed strong correlation (Fig. 4b). High-grade gold ores are mainly hosted by non-laminated, fracture altered quartz-pyrite veins, which interspersed with early laminated ore bodies, indicating possible superimposed mineralization (Fig. 5b). The geology, occurrence of the orebody, and alteration suggest that the mineralization is dependent on the subvolcanic magmatism-hydrothermal activity (Liang, 2018).

The principal ore minerals are pyrite, chalcopyrite, and sphalerite (Fig. 5d–j), with minor galena, bornite, tetrahedrite (Fig. 5m-n), and gold-bearing minerals, including calaverite, petzite, native gold, electrum, and so on (Fig. 5k, o). Gangue minerals mainly comprise quartz, barite, calcite, sericite, muscovite, chlorite, and K-feldspar (Fig. 5g and Fig. 6d–i). The ores mostly have sparse-dense disseminated (Fig. 5d), massive structures (Fig. 5e), stratiform-like (Fig. 5f), and veined (Fig. 5h). The paragenetic relationship between different minerals mainly consists of metasomatic relict (Fig. 5j, o), eutectic (Fig. 5m-n), and inclusion textures (Fig. 5k). The tuff and pyroclastic rocks were widely metasomatized by hydrothermal fluids with formation of a lot of disseminated and veined pyrite and chalcopyrite (Fig. 5d, h, n). Cu-Zn orebodies are mainly massive, stratiform-like and disseminated in tuff with minor galena and tetrahedrite (Fig. 5a-f, m-n). The Au unevenly enrich in the massive and veined orebodies, and coexist with pyrite or chalcopyrite (Fig. 5k, o).

Wall rock alteration in Huangtan is pervasive and is dominated by silicification (Fig. 6a-f), epidotization (Fig. 5a), sericitization (Fig. 6d), chloritization (Fig. 6e), muscovitization (Fig. 6f), carbonatization (Fig. 6g, h) and phyllic alteration (Fig. 6a–d). As the foremost alteration type, silicification and pyritic phyllic alteration mainly occurs within the orebodies and is characterized by abundant quartz associated with sericite, pyrite, muscovite and elemental sulfur (Fig. 6a–c). They are spatially and temporally associated with high-grade gold mineralization. Epidotization sericitization and chloritization mainly occurs outside of the pyritic phyllic alteration zone and are closely associated with the tuff surrounding orebodies. Late carbonatization is widespread with in the surrounding volcanic rocks as irregular veinlets. Besides, there are also many other altered minerals in and around the hydrothermal channel, such as alunite, smectite, K-feldspar, zeolite, limonite, and so on (Fig. 6a–c, i).

The field geology, mineral assemblages, paragenetic sequence, and ore fabrics relationships at Huangtan record a sequence of fluid-flow events. The mineralogy and associated wall-rock alterations are briefly summarized in Fig. 7, with a framework of four main paragenetic stages (S1–S4): diagenetic preore or hydrothermal early ore-stage (S1); hydrothermal main ore-stage (S2) associated with sub-stages S2-1 and S2-2; late ore-stage (S3); and supergene ore-stage (S4). The S1 is the earliest paragenetic stage occurred in the hydrothermal channel and is characterized by the formation of mineral assemblages consisting of pyrite, sphalerite with minor galena, bornite, tetrahedrite, calaverite, and electrum. Pyrite occurs as aggregates or subhedral-euhedral individual grains with round sphalerite, chalcopyrite and quartz occurred inside pyrite or along its margin as multiphase inclusions. Gold-bearing minerals usually occur as small polyphase inclusions in pyrite grains (Fig. 5k). S2-1 (prophase of the main ore-stage), represented by massive or irregular lodes of pyrite ± quartz associated with the pervasive pyritic

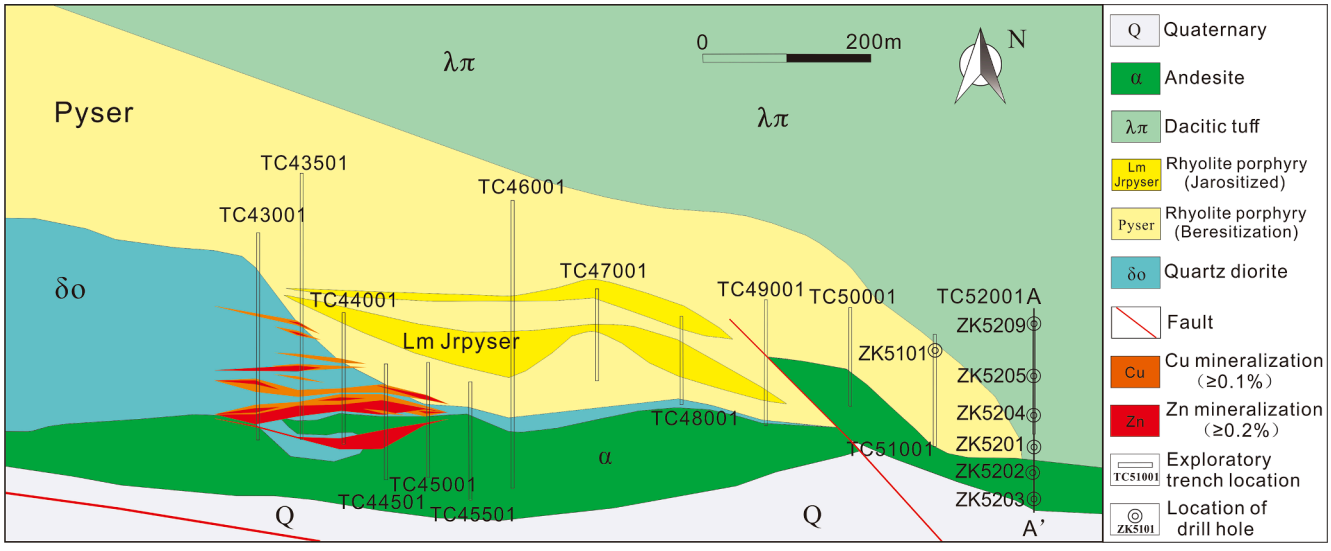

Fig. 3. Simplified geological map of the Huangtan deposit (modified from XXMCL, 2017).

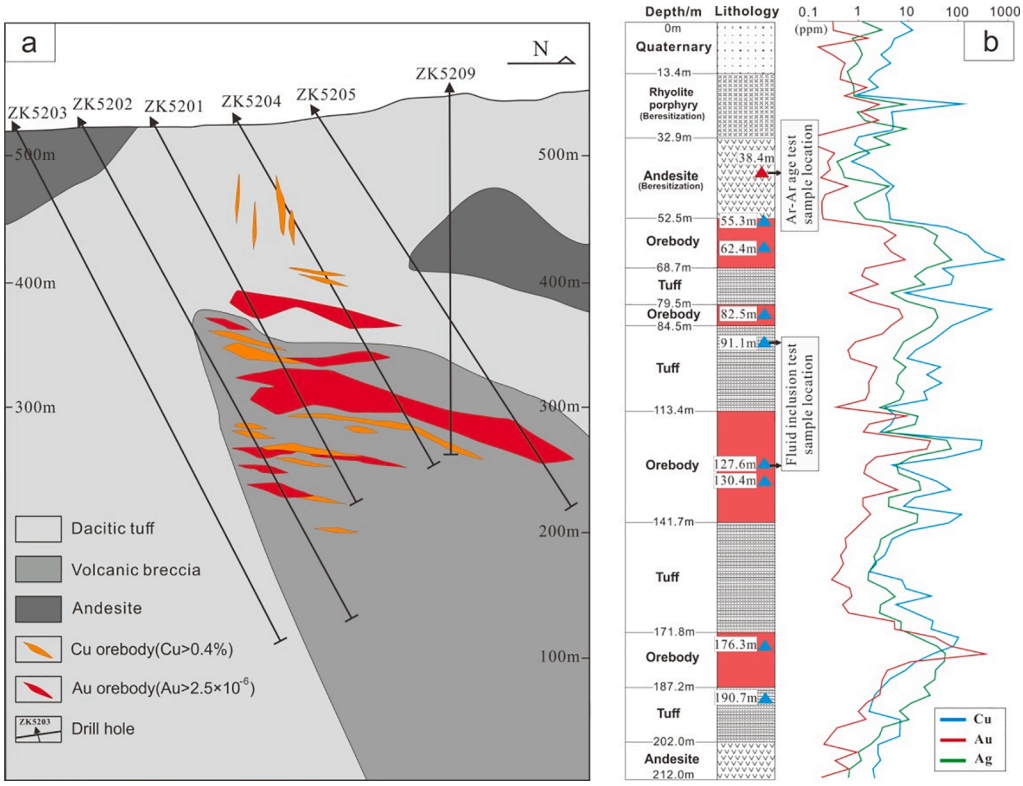

Fig. 4. a: Representative cross section of the Huangtan Au-Cu deposit (modified from He, 2019); b: The columnar section of drill hole ZK5101 and element content diagram from the Huangtan deposit.

phyllic alteration (Fig. 5e, l); S2-2 (late of the main ore-stage) is the main metallogenic stage of Cu, Zn, and Au, represented by irregular to banded pyrite ± chalcopyrite ± sphalerite ± electrum ± quartz ± barite veins cutting the propylitic alteration assemblage (Fig. 5f–h, m–o). The natural gold and electrum at this stage are mainly associated with chalcopyrite and distributed on the margins of pyrite particles (Fig. 5o); S3 (late-ore stage) is dominated by recrystallized veined quartz with minor sulfide minerals, and some calcite ± hematite veins with clear low temperature altered mineral assemblage (Fig. 5i and Fig. 6g–h); S4 (supergene ore-stage) is characterized by oxide mineralization in shallow orebodies, including abundant limonite, malachite, jarosite and other supergene minerals (Fig. 6a–c, i).

4. Sampling and analytical methods

4.1. Muscovite $^{40}Ar/^{39}Ar$ geochronology

One sample of muscovite for $^{40}Ar/^{39}Ar$ dating was collected from the pyritic phyllic alteration zone of late ore S3 within the drill hole ZK5101 (38.4 m) (Fig. 4b). Muscovite grains were cleaned by ultrasonic treatment in distilled water. Single-step laser fusion $^{40}Ar/^{39}Ar$ data for individual muscovite grains were collected at the Columbia University Lamont-Doherty Earth Science Observatory (LDEO). Mica samples and monitoring samples were irradiated in the Cd-lined, in core facility (CLICIT) at the Oregon State reactor. The normalization of neutron flux was based on an analysis of the 523 Ma McClure Mountain hornblende sample (Renne et al., 1998). CO_2 laser fusion was performed in the laboratory, and the VG5400 inert gas mass spectrometer was used to process single-particle samples for single-step laser melting $^{40}Ar/^{39}Ar$ determination. Sufficient sample particles and their one-step fusion were used to determine the $^{40}Ar/^{39}Ar$ age generation. Details of the procedures for irradiation and analysis, and values used to correct for interfering nuclear reactions are similar to those given by Renne et al., (1998).

4.2. Fluid inclusion analytical methods

Fifteen samples for fluid inclusion analysis were collected from the main orebodies and typical drilled cores (ZK5101, ZK5102, ZK5353 and ZK5352), including four quartz and one barite samples representing S1, three quartz and one barite samples for S2, and three quartz and two calcite samples for S3 (Fig. 9). The microthermometric study was carried out at the laboratory for fluid inclusions, China University of Geosciences (Wuhan), using a Linkam GP600 heating-freezing system mounted on an Olympus-BX51 infrared microscope with a temperature range of −196 °C to +600 °C. The estimated precision of the measurements is ±0.1 °C for temperatures lower than 31.5 °C, ±1 °C for the interval of 31.5–400 °C, and ±2 °C for temperatures higher than 400 °C, respectively. Fluid salinities of the NaCl-H_2O system were calculated utilizing the final melting temperatures of ice (Bodnar, 1993). All microthermometry results of fluid inclusions are obtained by conducting experiments on fluid inclusion assemblages based on detailed petrographic observations. The micrographs were taken by a monitor QIMAGING MP5.0 cooled RTV under plane polarized light and U-V light.

Representative samples for composition analysis were analyzed using a LABRAM RM-1000 Raman microspectrometer at the analytical laboratory of China University of Geosciences (Wuhan) according to the method of Burke (2001). The spectral range falls between 50 and 4000 cm^{-1} for the analysis of CO_2, N_2, CH_4, and H_2O in the vapor and liquid phase.

4.3. Isotope analytical methods

Nine quartz samples from various types of quartz–sulfide veins in drill hole ZK5101 and ZK5352 were selected for hydrogen and oxygen isotope analyses, including four quartz samples from S1, three quartz samples from S2, and two quartz samples from S3 (Fig. 9a, c). In the selection of samples for testing, secondary quartz was avoided as far as

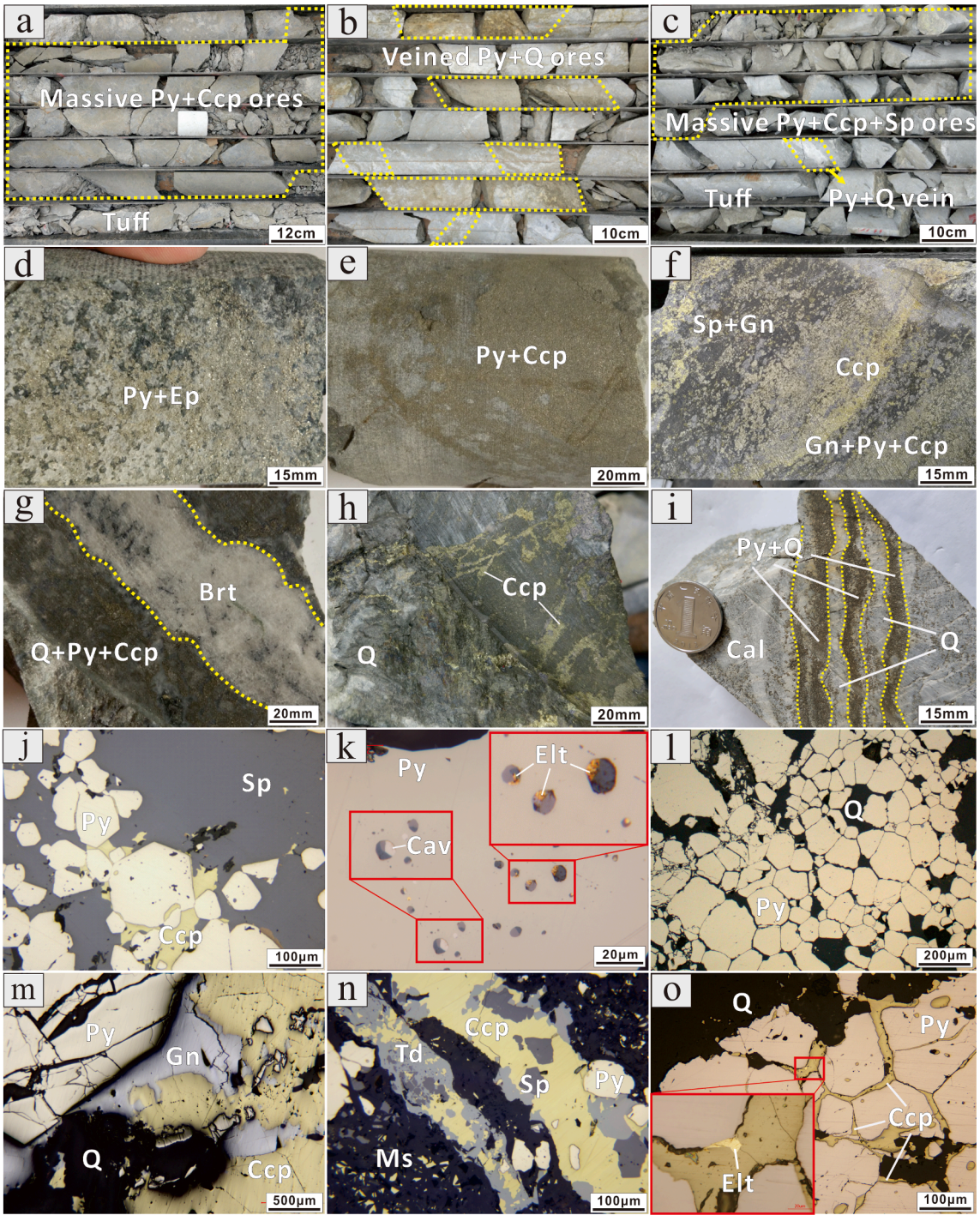

Fig. 5. Photographs and photomicrographs showing ore fabrics and mineral assemblages of the Huangtan Au-Cu deposit. a: Massive pyrite + chalcopyrite ores in the drill hole; b: Veined pyrite + quartz ores; c: Massive pyrite + chalcopyrite + sphaletite ores; d: Altered pyroclastic with disseminated pyrite in S1; e: Dense massive structure pyrite ore; f: Banded-stratoid structure of chalcopyrite + pyrite + galena ore in S2; g: Barite vein in S2 crosscut disseminated pyrite, chalcopyrite and quartz in S1; h: Stockwork chalcopyrite in S2 crosscut altered tuff; i: Veined and banded quarta + pyrite + calcite in S2-3; j: Subhedral pyrite and chalcopyrite replaced by sphalerite; k: Electrum-calaverite-chalcocite-sphalerite inclusions in pyrite particles; l: Dense quartz and pyrite in massive ores; m: Pyrite replaced by galena, chalcopyrite and quartz; n: Muscovite-polymetallic vein, including sphalerite, galena, chalcopyrite, tetrahedrite and pyrite; o: Pyrite particles replaced by chalcopyrite, electrum and quartz. Abbreviations: Q, quartz; Ep, epidote; Brt, barite; Ms, muscovite; Ccp, chalcopyrite; Py, pyrite; Gn, galena; Td, tetrahedrite; Cav, calaverite; Cc, chalcocite; Elt, electrum.

possible. The number of secondary fluid inclusions in the selected test samples is very limited, and its influence on the experimental results is not considered here. All the quartz samples, with sizes of 40–60 mesh, were prepared by careful handpicking under a binocular microscope to achieve a purity of 99%, which was followed by cleaning in doubly distilled water. Hydrogen and oxygen isotopes were analyzed on a

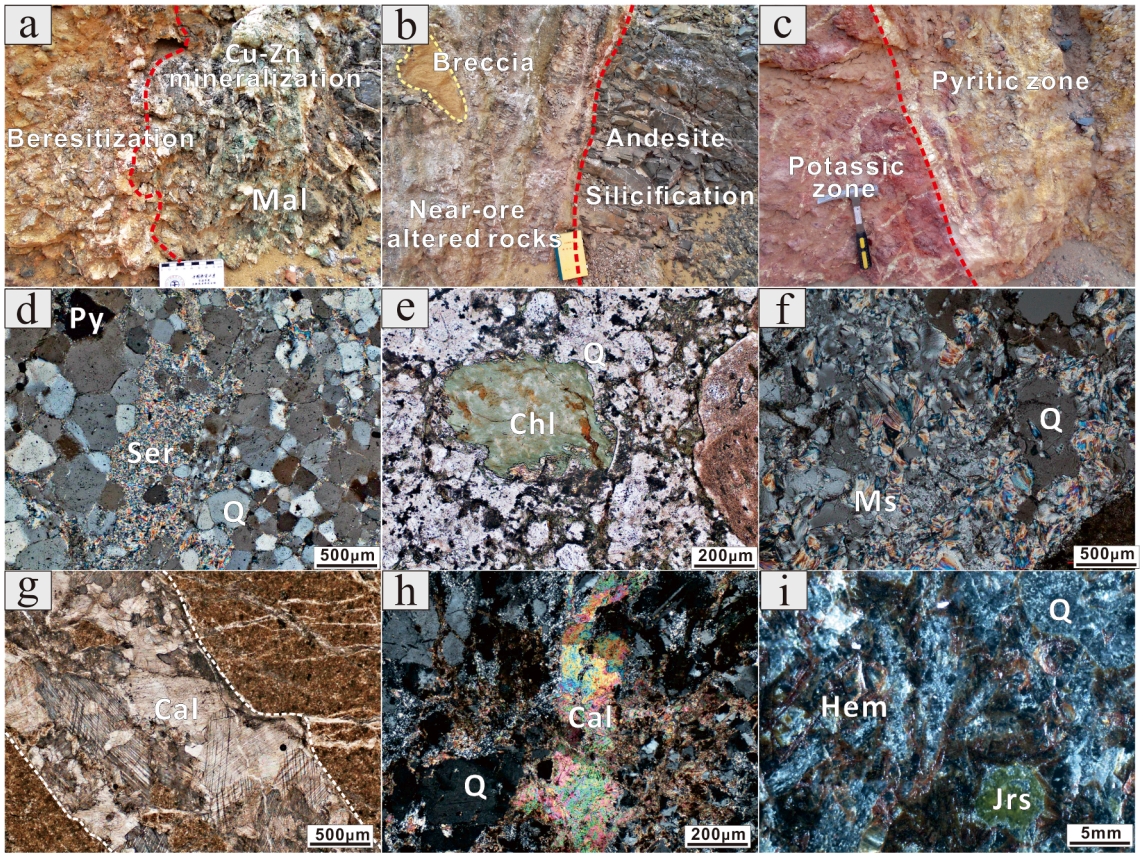

Fig. 6. Photographs and photomicrographs of alteration features from the Huangtan deposit. a: Cu-Zn mineralization and beresitization; b: Near-ore breccia and altered rocks at the hydrothermal channel site; c: Pyritic and potassic zone with argillic mineral assemblages, such as alunite ± smectite; d: Phyllic alteration in felsic volcanic rocks, comprising sericite, quartz, and pyrite; e: Silicification and chloritization in wall rock; f: Quartz and muscovite in sulfide vein; g-h: Calcite vein crosscut quartz, sericite and chlorite alteration in S3; i: Jarosite, limonite and quartz at the bottom of overlain layers (Oblique light). Abbreviations: Q, quartz; Py, pyrite; Cal, calcite; Chl, chlorite; Ser, sericite; Ms, muscovite; Jrs, Jarosite; Hem, limonite; Mal, malachite.

Finnigan-MAT 253 stable isotope ratio mass spectrometer. Using the fractionation formula stated by Clayton et al. (1972), the oxygen isotope ratios of water in balance with the minerals are determined. For the same samples, the hydrogen isotopic compositions of the fluid inclusions were analyzed. The results were normalized with Vienna-$_{SMOW}$ standards and the precisions were better than ±2‰ and ±0.2‰ for δD and $\delta^{18}O$, respectively.

Some typical sulfide and sulfate samples from the main Cu-Au orebody and gangues were chosen for analysis of sulfur and lead isotopes. Besides, six relevant igneous rock samples were also selected for lead isotope analysis. Sulfur isotopic ratios were calculated using the VCDT norm on a Delta-V plus mass spectrometer. Analytical precision and accuracy are higher than ±0.2‰. The lead isotope analyses were performed by using a thermal ionization mass spectrometry and the isotopic ratios of the measured Pb of the international standard NBS981 are around 0.1.

All monomineralic S-Pb-H-O analyses were carried out at the Analytical Laboratory of the Beijing Research Institute of Uranium Geology (BRIUG). Lead isotope analyses of whole-rock samples were carried out on a Neptune Plus MC-ICP-MS (Thermo Fisher Scientific, Dreieich, Germany) at the Wuhan Sample Solution Analytical Technology Co., Ltd, Hubei, China, using analytical procedures of Baker et al. (2004). In situ sulfur isotope analyses were conducted using the Resolution-S155 excimer ArF Laser ablation system at the State Key Laboratory of Geological Processes and Mineral Resources (GPMR), China University of Geosciences (Wuhan). Specific analytical conditions and procedures used are given in Zhu et al. (2016).

5. Analytical results

5.1. Muscovite $^{40}Ar/^{39}Ar$ geochronology

The Ar-Ar age spectra of the analyzed hydrothermal muscovite are presented in Fig. 8, and the corresponding results of the Ar-Ar data are summarized in Table 1. A muscovite sample (TC4401-1) from the late ore stage (S3) coexisting with pyritic phyllic alteration was collected for dating (Fig. 6a). It was incrementally heated with eleven steps from 400 °C to 1400 °C and yielded a ^{40}Ar-^{39}Ar plateau age of 414.4 ± 0.4 Ma, which represents 34% of the cumulative ^{39}Ar released during analysis (Fig. 8a). This age accounts for only three of the eleven steps, but it can still extract useful mineralization information. The age spectrum shows excess argon (^{40}Ar) or partial loss of minor amounts of radiogenic argon component in the first five steps (Dalrymple and Lanphere, 1969; Vasconcelos, 1999). Besides, this sample also yielded an isochron age of 414.4 ± 6.2 Ma, with an intercept corresponding to the atmosphere on the $^{40}Ar/^{36}Ar$ axis (i.e., $^{40}Ar/^{36}Ar = 257$; Fig. 8b).

5.2. Microthermometry and salinity

5.2.1. Petrography of fluid inclusions (FIs)

Abundant FIs trapped in the quartz-bearing veins, barite and calcite from different mineralization stages were observed (Fig. 10), and only primary FIs were analyzed here, according to the textural criteria of Roedder (1984). Representative samples of each stage were chosen for temperature measurement of FIs, including 10 quartz samples, 2 barite samples and 2 calcite samples (Table 2). These undeformed and not

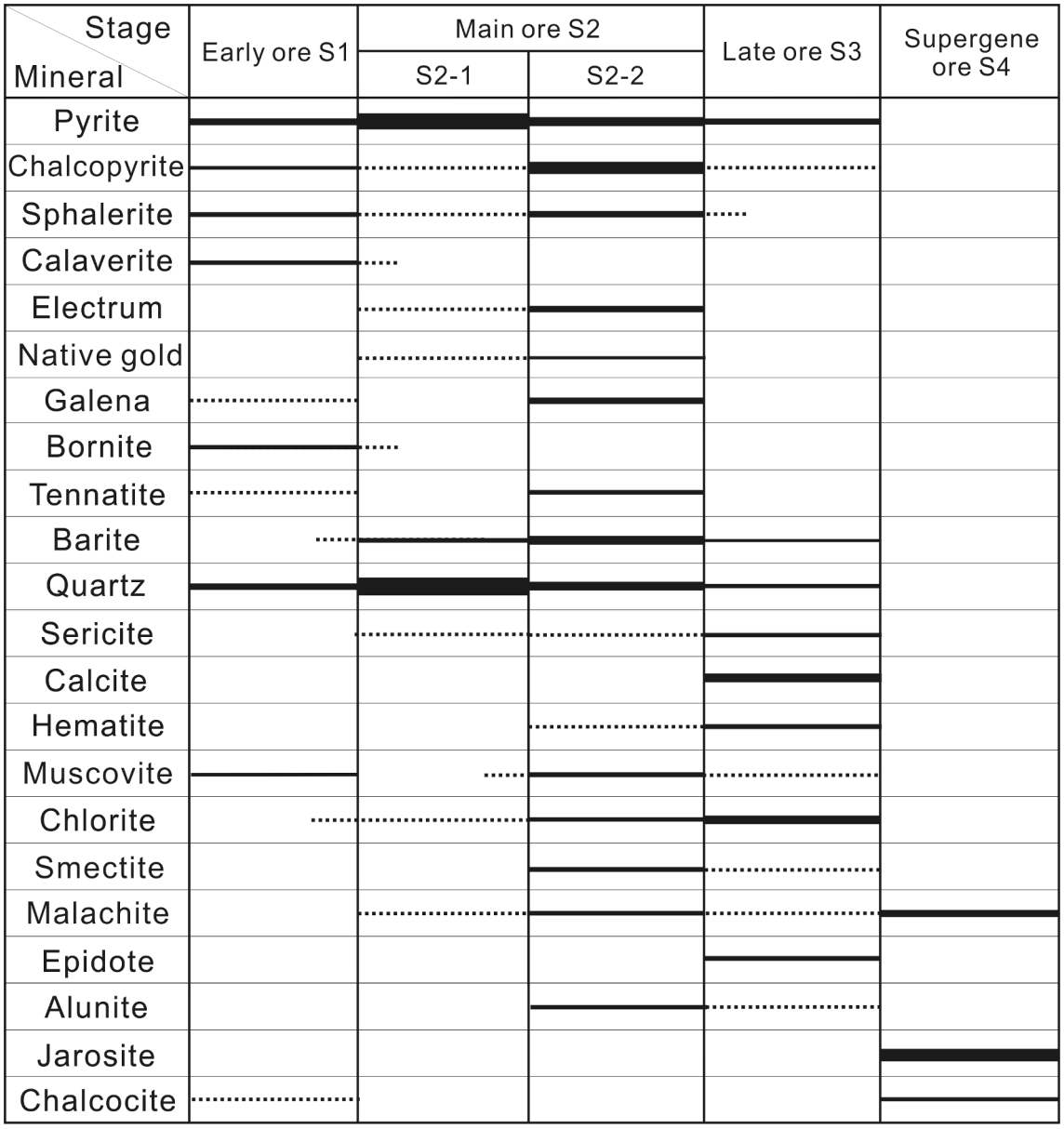

Fig. 7. Paragenetic sequence of ore and gangue minerals for the Huangtan Au-Cu deposit.

recrystallized samples are derived from different mineralization stages, including primary and pseudosecondary FIs (Fig. 9a–d). Secondary fluid inclusion data has been eliminated. On the basis of their phase proportion at 25 °C (room temperature), and phase transitions during heating and cooling, four types of FIs were revealed: (1) Liquid-rich (L-type) two-phase FIs are the most common type from the different paragenetic stages. They have rounded, or irregular shapes (Fig. 10a–d, h–l) and range from 5 to 15 μm in size (Table 2). The vapor bubbles are relatively small, ranging from 5 to 50 vol% of the fluid inclusion volume (Fig. 10a–d, h–l). (2) Liquid-rich, solid-bearing (S-type) three-phase inclusions have opaque or transparent daughter minerals (Fig. 10a, f-g), and were generally trapped during the early and main ore stages. (3) Vapor-rich (V-type) two-phase FIs are detected in S1 to S2 quartz veins and have 50 to 95 vol% vapor bubbles (Fig. 10e). They are ellipsoidal, irregular, and fusiform in shape and appear gray-colorless and transparent with the same dimensions as L-type FIs. (4) Mono-phase liquid (M-type) FIs generally appear as one phase (H_2O) at room temperature (Fig. 10j). Besides, the gas phase of a few early Fls (S1-S2) shows varying shades of gray, but no three-phase FIs containing liquid phase CO_2 are found.

5.2.2. *Microthermometry results*

The microthermometric data and calculated parameters for FIs are summarized in Table 2 and graphically illustrated in Fig. 11 and Fig. 13a, which show the linkage between mineral assemblages, metallogenic stages and physico-chemical conditions. FIs in S1 are dominated by L- and V-types with minor S-type. The L-type FIs homogenized to liquid at 263–379 °C (average = 308 °C, n = 90), with densities ranging from 0.76 to 0.86 g/cm^3 (Fig. 11a). Their ice-melting temperatures are between −10.2 °C and −3.3 °C, corresponding to salinities of 5.3 to 14.2 wt% NaCl equiv (Fig. 11b). The V-type fluid inclusion assemblages homogenize to vapor at temperatures of 305 °C to 348 °C (average = 324 °C, n = 18), with densities ranging from 0.67 to 0.78 g/cm^3. They have ice-melting temperatures of −9.2 °C to −5.9 °C, corresponding to salinities of 9.0–13.1 wt% NaCl equiv. The S-type FIs contain some transparent or opaque daughter minerals that do not disappear in the heating process, and thus unable to enumerate the homogenization temperatures uniform temperatures and salinities.

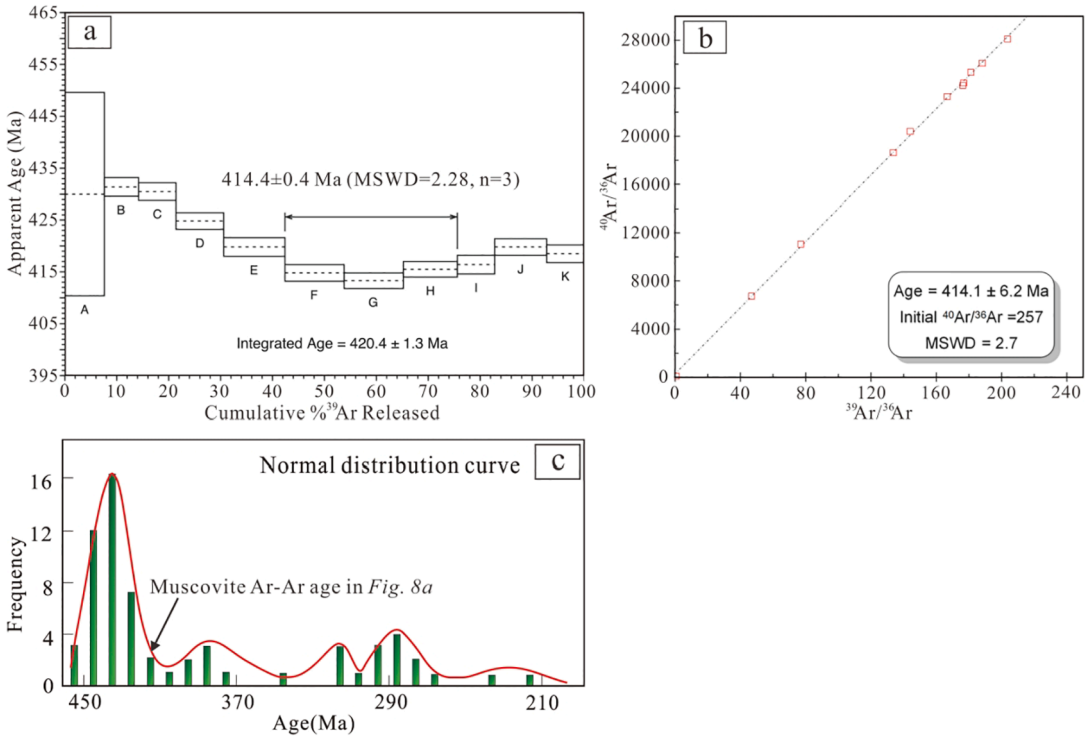

Fig. 8. ^{39}Ar–^{40}Ar age spectra (a) and isochron age (b) of the hydrothermal muscovite from the Huangtan deposit; c: isotopic ages normal distribution curve of Cu-dominant deposits and causative magmatism in the Kalatag district (modified from Deng et al., 2020).

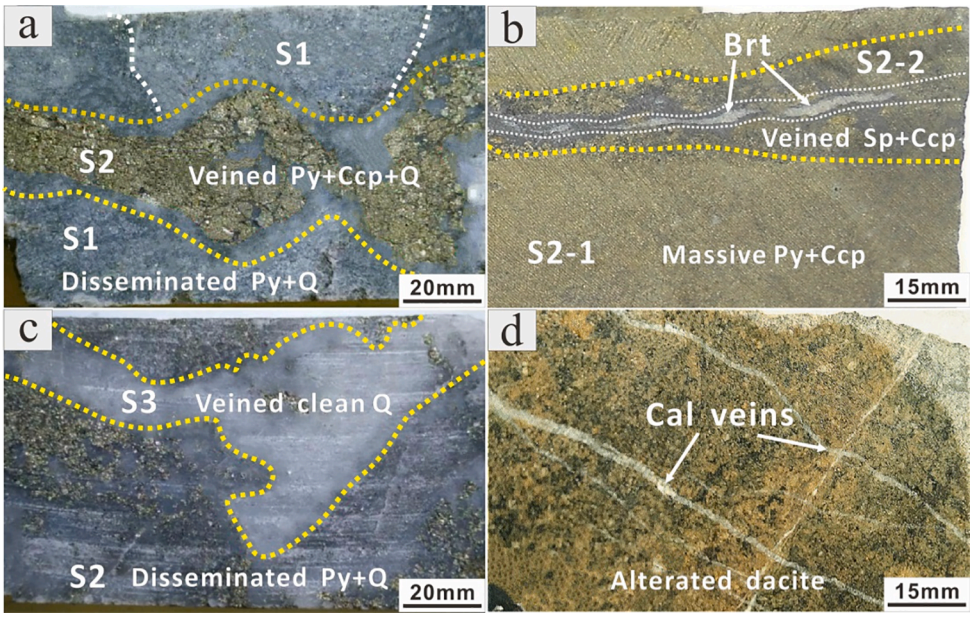

Fig. 9. Photographs showing Cu-Au ore fabrics and vein cutting relationships of the Huangtan deposit. a: Disseminated pyrite-bearing quartz veins (S1) hosted in the tuff at footwall of ore bodies cutted by pyrite + chalcopyrite + quartz vein of S2; b: Veined sphalerite + chalcopyrite + barite (S2-2) cutting S2-1 massive pyrite + chalcopyrite; c: S3 veined clean quartz cutting S2 disseminated pyrite + gray quartz in the dacitic tuff; d: S3 calcite veinlet in the alterated dacite on the hanging wall. Abbreviations: Q, quartz; Brt, barite; Cal, calcite; Ccp, chalcopyrite; Py, pyrite; Sp, sphalerite.

The S2 quartz veins are mainly comprised of L- and V-types FIs. The L-type FIs homogenized to liquid at temperatures of 188–292 °C (average = 240 °C, n = 54; Fig. 11c, Table 2). Their final melting temperatures of ice range from −7.2 °C to −1.6 °C, with calculated salinities of 2.8–10.7 wt% NaCl equiv and estimated to be 0.83–0.94 g/cm^3 (Fig. 13a, Table 2). The V-type FIs yield ice-melting temperatures range from −6.9 to −3.4 °C, corresponding to salinities of 5.5–10.4 wt% NaCl equiv. Their homogenization temperatures range from 247 °C to 275 °C (average = 258 °C, n = 11; Fig. 11c, d), with densities of 0.81–0.87 g/cm^3 (Fig. 13a). A small amount of sulfide-bearing FIs (cubic crystal; Fig. 10f) found at this stage were also failed to measure the homogenization temperature.

The S3 quartz and calcite veins mainly contain L- and M- type FIs, and the L-type homogenized to the aqueous liquid phase at temperatures between 118 °C and 198 °C (average = 158 °C, n = 73), with densities ranging from 0.90 to 1.02 g/cm^3. The final ice-melting temperatures vary from −10.2 °C to −0.2 °C with calculated salinities of 0.3 to 14.1 wt % NaCl equiv (Fig. 11e, f, and Fig. 13a).

5.3. Laser Raman spectroscopy

Representative FIs from different stages were chosen for laser Raman

Table 1
40Ar/39Ar stepwise heating data of sericite from the Huangtan deposit.

T(°C)	Ca/K	Cl/K	$^{40*}Ar/^{39}Ar$ (F)	$^{36}Ar/^{39}Ar$	$\%^{40}Ar^*$	$\%^{39}Ar$ in step	Mol ^{39}Ar	Cum.% ^{39}Ar	Age (Ma)	±2σ
400	0.04458	0.0284	143.65593	1.88273	20.4	7.7	0.1948	7.7	429.82793	9.80898
500	0.06667	−0.00344	144.21996	0.021365	95.8	6.7	0.1678	14.4	431.3314	0.91802
600	0.02598	−0.00261	143.86788	0.012994	97.4	7.1	0.1789	21.5	430.39306	0.87343
700	0.00744	−0.00226	141.74223	0.006947	98.6	9.2	0.2309	30.7	424.71759	0.82116
800	0.00654	−0.00179	139.84923	0.005522	98.8	11.8	0.2976	42.5	419.64847	0.87795
900	0.00701	−0.00178	137.98653	0.004912	98.9	11.3	0.2854	53.8	414.64669	0.78872
1000	0.00647	−0.00182	137.43726	0.005673	98.8	11.5	0.2899	65.3	413.16918	0.75155
1100	0.00305	−0.00093	138.27584	0.005659	98.8	10.4	0.2616	75.7	415.42447	0.76769
1200	0.00577	−0.00385	138.62344	0.005315	98.9	7.2	0.1811	82.9	416.3585	0.87958
1300	0.00406	−0.00336	139.83314	0.006004	98.7	10	0.251	92.8	419.60531	0.80039
1400	0.00619	−0.00136	139.41117	0.007486	98.4	7.2	0.1804	100	418.47341	0.84598

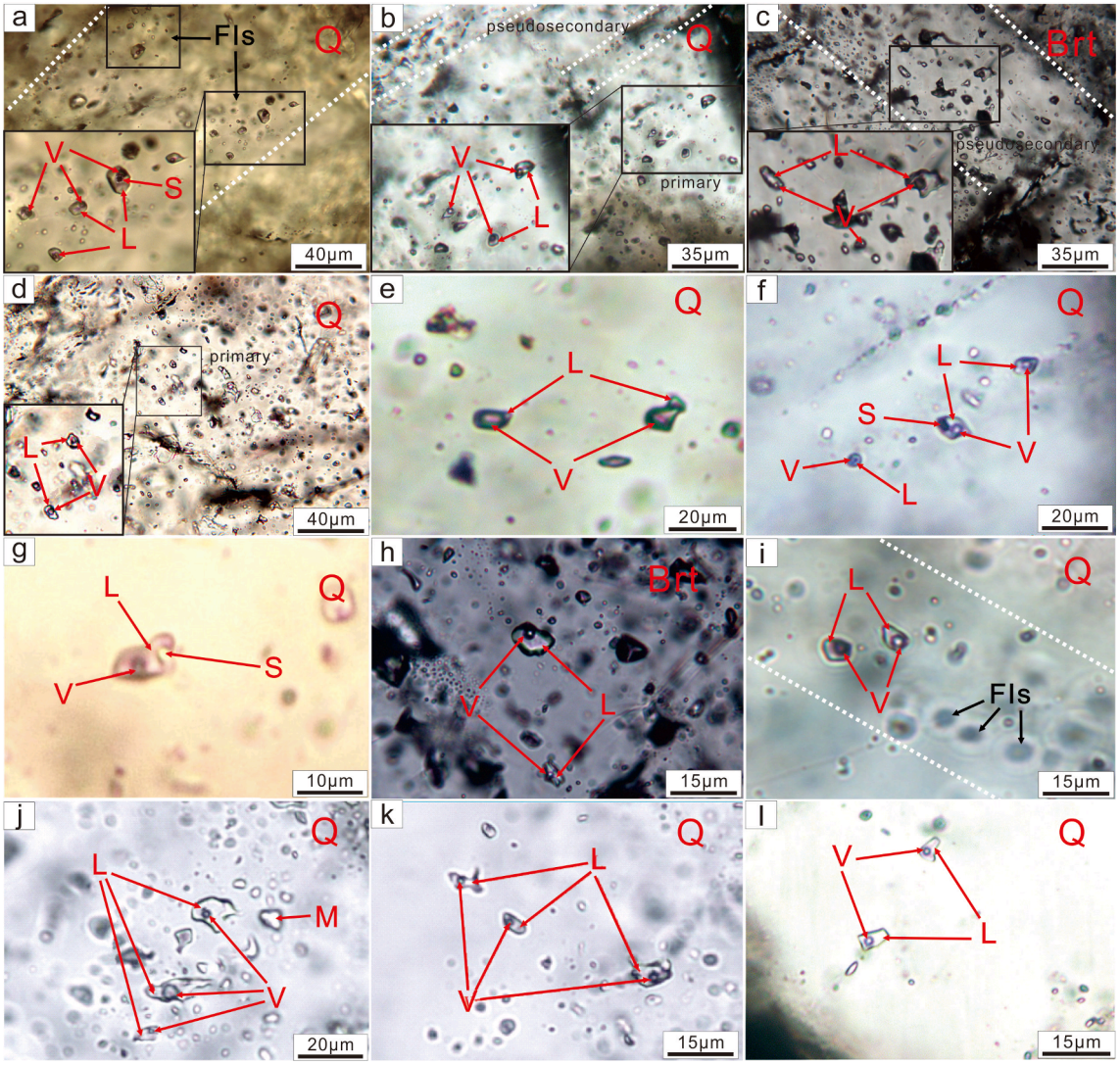

Fig. 10. Photomicrographs of different types of fluid inclusions (FIs) in different minerals. a-b: primary and pseudosecondary FIs in quartz from S1; c: pseudosecondary FIs in barite from S2; d: primary FIs in quartz from S3; e: the V-type FIs in the S1 quartz; f: the L-type and metal daughter mineral-bearing FIs (S-type) from S1-2 quartz; g: the sulfate (SO_4^{2-}) daughter mineral-bearing multiphase FIs (S-type) from S1 quartz; h: the L-type FIs in the S2 barite; i: the pseudosecondary L-type FIs in the S2 quartz; j: the pseudosecondary L- and M-type FIs in the S3 quartz; k: the L-type FIs in the S3 quartz; l: the L-type FIs in the S3 calcite. Abbreviations: S, solid; V, vapor; L, liquid phases; M, Mono-phase; Q, quartz; Brt, barite; Cal, calcite.

spectroscopy to restrict their compositions, and parts of the spectra are shown in Fig. 12 Laser Raman analyses of individual FIs indicate that the vapor phases present at L- and V-type inclusions in S1 are H_2O and CO_2 with minor amounts of CH_4 and N_2 (Fig. 12a–c). The gas phases in the FIs from the quartz–polymetallic sulfide veinlets (S2) are mainly composed of H_2O, CH_4 and CO_2 (Fig. 12d-e). Besides, within S1 to S2, the number of FIs detected with CO_2 signal is very limited. The gas components in the FIs from S3 primarily include H_2O, with minor CH_4 (Fig. 12f).

Table 2
Microthermometric data of fluid inclusions of the Huangtan deposit.

Sample	Stage	Host mineral	FI Types	Homogenization state	Size/μm	Tm(ice)/ °C (N)	Th/ °C (N)	Salinity(wt.% NaCl eq)
HT-22	S1	Quartz	L + V	Liquid or Vapor	5–12	−10.2 to −4.5(13)	305–348(20)	7.2–14.2
HT3-27		Barite	L + V	Liquid or Vapor	6–15	−8.2 to −3.3(10)	308–379(21)	5.3–11.9
HT-21		Quartz	L	Liquid	5–10	−8.5 to −4.6(8)	263–312(26)	7.3–12.3
HT-18		Quartz	L + V	Liquid	5–12	−6.9 to −3.4(4)	287–345(29)	5.6–10.4
HT-17		Quartz	L	Liquid	5–15	−7.5 to −5.2(7)	281–325(12)	8.1–11.1
HT2-24	S2	Barite	L + V	Liquid or Vapor	8–16	−7.2 to −3.7(10)	235–292(20)	6.0–10.7
HT-15		Quartz	L	Liquid	5–10	−6.5 to −2.6(6)	188–252(14)	4.3–9.9
HT-10		Quartz	L + V	Liquid or Vapor	5–13	−6.9 to −3.4(11)	204–285(18)	5.6–10.4
HT-5		Quartz	L	Liquid	8–12	−4.2 to −1.6(7)	192–245(13)	2.8–6.7
HT-2	S3	Quartz	L	Liquid	5–10	−10.2 to −2.3(10)	135–198(18)	3.9–14.1
HT-4		Quartz	L	Liquid	6–12	−5.2 to −1.9(8)	155–182(15)	3.2–8.1
HT2-9		Quartz	L	Liquid	5–12	−5.6 to −1.4(5)	148–187(12)	2.4–8.7
HT4-6		Calcite	L	Liquid	6–10	−3.7 to −0.4(9)	118–165(15)	0.7–6.0
HT2-15		Calcite	L	Liquid	5–15	−3.2 to −0.2(11)	132–178(13)	0.4–5.3

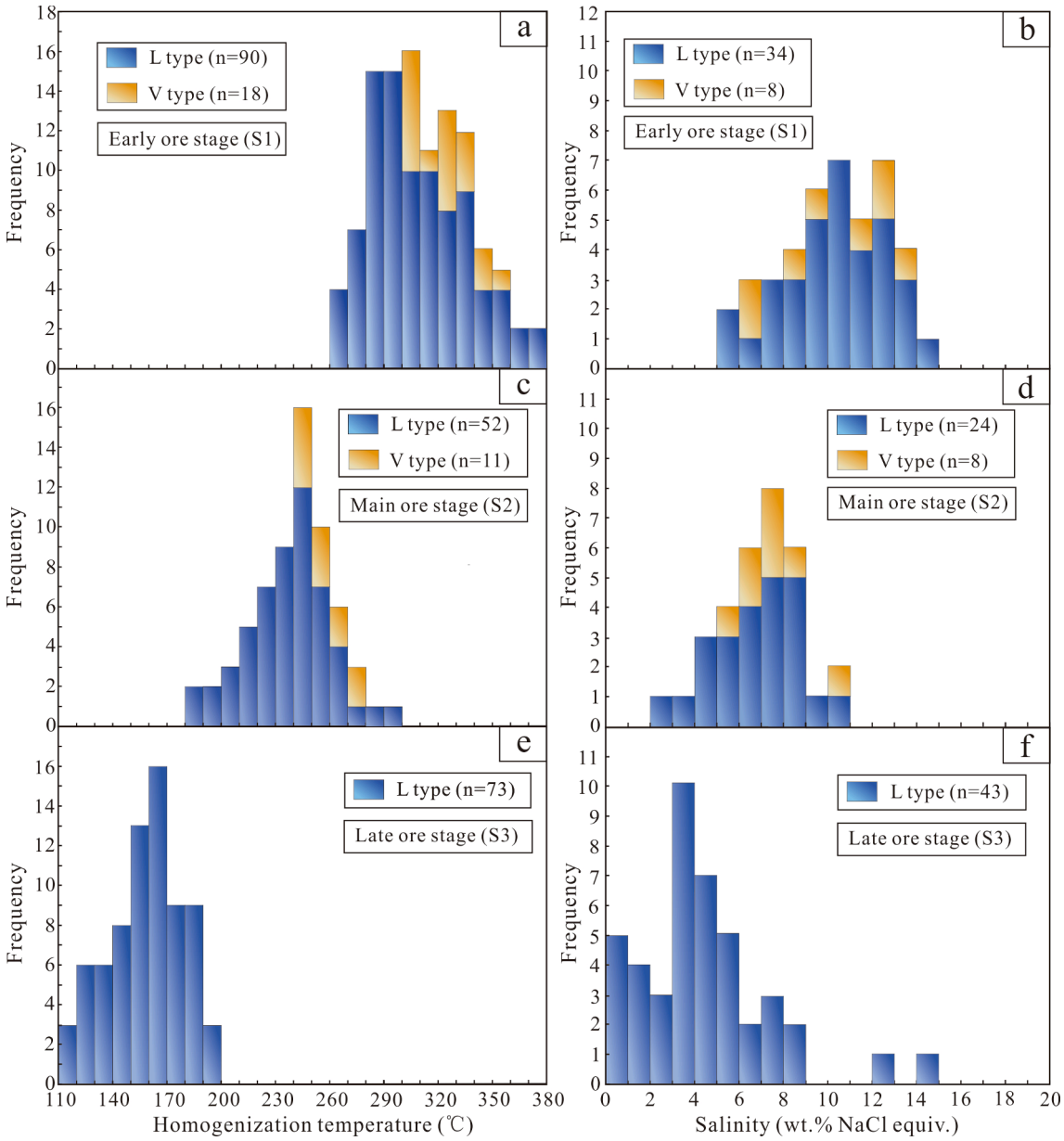

Fig. 11. Histograms of homogenization temperature (a, c and e) and salinities (b, d and f) for all types of inclusions in different ore stages of Huangtan deposit.

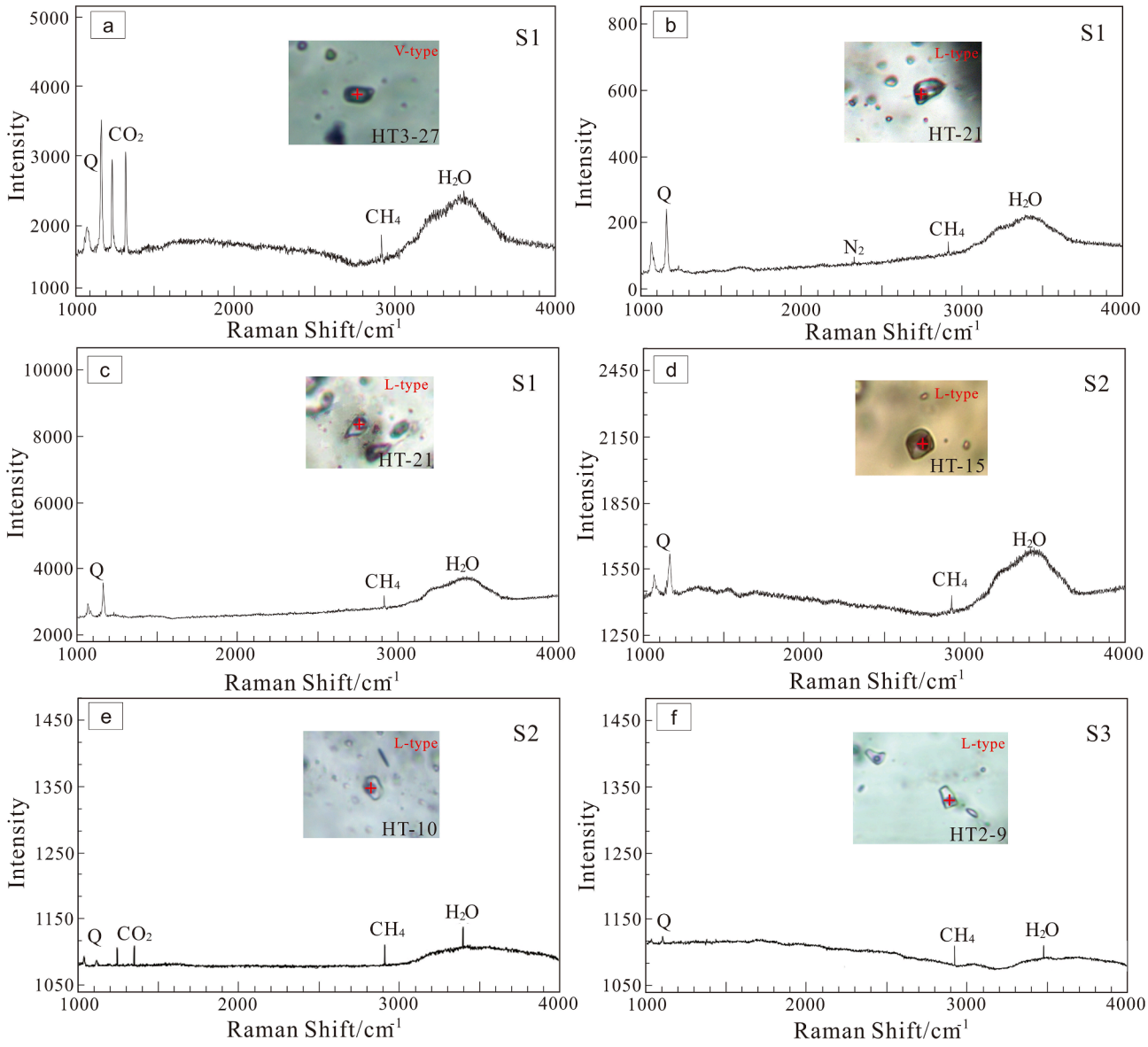

Fig. 12. Representative Raman spectra of FIs in the Huangtan deposit. a: CH_4, CO_2 and H_2O spectra of vapor in V-type FIs of S1 quartz; b-c: CH_4 and H_2O spectra of vapor in L-type FIs in S1 quartz; d-e: CH_4, CO_2 and H_2O spectra of vapor in L-type FIs in S2 quartz; f: CH_4 and H_2O spectra of vapor in L-type FIs in S3 quartz.

5.4. Oxygen and hydrogen isotopes

The H-O isotopic compositions are listed in Table 3 and shown in Fig. 13b. The calculated $\delta^{18}O_{H2O}$ values of water in equilibrium with quartz are based on the fractional equilibrium formulae of Clayton et al. (1972), with the average Th (°C) of FIs in quartz from every stage. Test results show that calculated $\delta^{18}O_{H2O}$ values from S1 to S3 of ore-fluids range from −6.1 to 5.6‰, and overlap those of the Cu-polymetallic deposits in the Kalatag ore field (−5.8 to 5.9‰; Deng et al., 2020). The measured δD values of the quartz samples for S1, S2, and S3 are −66.8 to −60.2‰, −58.4 to −55.4‰ and −56.1 to −53.9‰, respectively (Fig. 13b; Table 3).

5.5. Sulfur and lead isotopes

The sulfur and lead isotopic data of the different minerals are summarized in Tables 4 and 5, and are plotted in Figs. 14 and 15, respectively. Sulfide and sulfate minerals including pyrite, chalcopyrite, sphalerite, and barite were selected for sulfur isotope analysis. The range of $\delta^{34}S$ values for all the sulfides is relatively restricted (Fig. 14a). Monomineralic and in-situ sulfur isotope test results show that the pyrite $\delta^{34}S$ values range between −3.16 and +0.50‰, with an average of −0.98‰ (n = 26). The $\delta^{34}S$ values of chalcopyrite samples range from −5.25‰ to −1.41‰, with an average of −2.73‰ (n = 5) The $\delta^{34}S$ values for sphalerite range between −3.11 and −2.01‰, typically averaging −2.62‰ (n = 4; Fig. 14a, b). The $\delta^{34}S$ values of barite samples range from 29.60‰ to 30.80‰, with an average of 30.07‰ (n = 3; Fig. 14a, b). These $\delta^{34}S$ values exhibited a trend of $\delta^{34}S_{pyrite} > \delta^{34}S_{sphalerite} > \delta^{34}S_{chalcopyrite}$, which is consistent with sulfur isotopic equilibrium conditions. The $\delta^{34}S$ values of barite are highly positive, indicating that it mainly comes from seawater, which is consistent with the Early Paleozoic seawater evaporative salt-sulfur isotope given by Claypool et al. (1980). Moreover, all of these minerals are comparable to the $\delta^{34}S$ values for most typical VMS deposits (Fig. 14b).

The Pb isotopic compositions of five pyrite samples show that $^{206}Pb/^{204}Pb$ ratios ranging from 17.868 to 18.456, $^{207}Pb/^{204}Pb$ from 15.448 to 15.499, and $^{208}Pb/^{204}Pb$ from 37.350 to 37.619 (Table 5). Two chalcopyrite samples have $^{206}Pb/^{204}Pb$ ratios of 17.878 to 17.886, $^{207}Pb/^{204}Pb$ ratios of 15.446 to 15.460, and $^{208}Pb/^{204}Pb$ ratios of 37.351 to 37.397. Six igneous rock samples from the Kalatag district have Pb

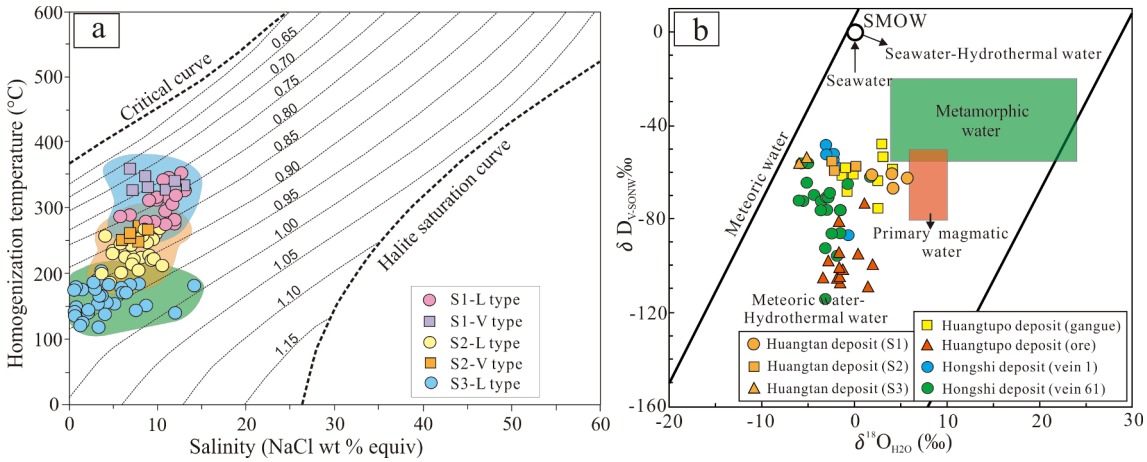

Fig. 13. a: Homogenization temperature vs. salinity diagram of FIs in different stages from the Huangtan deposit (modified after Wilkinson, 2001); b: Hydrogen (H) and oxygen (O) isotopic compositions of the ore fluids for the Kalatag goldfield (H-O isotopic data of the Huangtupo and Hongshi deposits were obtained from Mao et al., 2019; Deng et al., 2020); The primary magmatic and metamorphic water boxes are from Taylor (1974); SMOW = standard mean ocean water.

Table 3
Hydrogen and oxygen isotopic data of fluids from the Huangtan deposit.

Sample	Mineral	stage	$\delta^{18}O_{V\text{-}SMOW}$(‰)	$\delta D_{V\text{-}SMOW}$(‰)	$\delta^{18}O_{H2O}$(‰)	T (°C)
HT-22	Quartz	S1	10.6	−62.5	5.6	360
HT-21	Quartz	S1	9.6	−66.8	4.0	340
HT-18	Quartz	S1	10.3	−60.2	3.9	314
HT-17	Quartz	S1	9.2	−61.2	1.7	285
HT-15	Quartz	S2	9.5	−56.4	−0.2	235
HT-10	Quartz	S2	7.7	−58.4	−2.4	228
HT-5	Quartz	S2	8.9	−55.4	−2.5	205
HT-4	Quartz	S3	7.2	−53.9	−5.5	185
HT-2	Quartz	S3	7.0	−56.1	−6.1	180

isotope ratios of $^{206}Pb/^{204}Pb = 18.205$ to 19.495, $^{207}Pb/^{204}Pb = 15.536$ to 15.575, and $^{208}Pb/^{204}Pb = 38.043$ to 38.491. As shown in Fig. 15, all of these Pb isotopic data at Huangtan show analogous compositions.

6. Discussion

6.1. Timing of Au-Cu mineralization

Four distinct episodes of mineralization and magmatism have been identified in the Kalatag district: 450–430 Ma, 390–380 Ma, 320–300 Ma, 280 Ma, and a series of age data confirm that the Late Ordovician-Silurian is the most important mineralization period in the Kalatag area (Fig. 8c; Deng et al., 2020; Sun et al., 2020). For example, Mao et al. (2019) and Deng et al. (2016a) reported a reliable Re-Os isochron age of Huangtupo and Hongshi deposits, which is 436.1 ± 2.3 Ma and 429.8 ± 5.9 Ma, respectively. Reliable zircon and Ar-Ar ages also confirm that important Cu-Zn-Au mineralization occurred during this period (Deng et al., 2016b). The mineralization age of Huangtan is constrained by the age of the dacitic tuff at the bottom of the orebody (437.9 ± 6.6 Ma) and the Re-Os ages of auriferous pyrite (437.9 ± 6.6 Ma; Sun et al., 2020). Deposits formed contemporaneously with the Huangtan deposit are mainly of VMS type (Huangtupo) and hydrothermal vein-type (Hongshi), while the Huangtan and Huangtupo deposit have similar deposit characteristics and close spatio-temporal relationship, showing the characteristics of VMS deposit. Our muscovite sample has a ^{40}Ar-^{39}Ar plateau age of 414.4 ± 0.4 Ma, with a corresponding isochron age of 414 ± 6.2 Ma. This ^{40}Ar-^{39}Ar plateau age is taken as the age of mica-cization proximal to the late quartz-sulfide ores and represents the upper age limit of shallow hydrothermal alteration and Au-Cu mineralization, which is consistent with the age of Huangtan mineralization (437.9 ± 6.6 Ma; Sun et al., 2020). Moreover, the first three stages of this age spectrum are coincidentally consistent with the main metallogenic epoch of the Huangtan deposit and may record corresponding thermal metallogenic events. In addition, geological evidence shows that the

Table 4
Sulfur isotopic composition of sulfides and sulfates from the Huangtan deposit.

No.	Sample	Mineral	$\delta^{34}S_{V\text{-}CDT}$(‰)	Remarks	No.	Sample	Mineral	$\delta^{34}S_{V\text{-}CDT}$(‰)	Remarks
1	5101-7B-3	Pyrite	−2.58	in-situ	20	5101-7B-6	Sphalerite	−3.05	in-situ
2	5101-7B-5	Pyrite	−2.19		21	5101-7B-4	Sphalerite	−2.30	
3	5101-7B-9	Pyrite	−3.16		22	5101-7B-7	Chalcopyrite	−5.25	
4	5101-7B-10	Pyrite	−0.56		23	5101-7T-3	Chalcopyrite	−1.41	
5	5101-7B-11	Pyrite	−0.81		24	5101-10-1	Chalcopyrite	−1.94	
6	5101-7B-12	Pyrite	−0.21		25	5101-13-4	Chalcopyrite	−2.74	
7	5101-7B-13	Pyrite	−0.59		26	5101-13-5	Chalcopyrite	−2.31	
8	5101-7T-1	Pyrite	−0.60		27	ZK2-5352-20B	Barite	29.80	
9	5101-7T-2	Pyrite	−0.57		28	ZK2-5352-20B	Barite	29.60	
10	5101-7T-4	Pyrite	−0.65		29	ZK2-5352-20B	Barite	30.80	
11	5101-7T-5	Pyrite	−0.67		30	5101-4	Pyrite	−1.9	monomineral
12	5101-13-1	Pyrite	−0.81		31	5101-6	Pyrite	−1.4	
13	5101-13-2	Pyrite	−0.70		32	5101-10	Pyrite	−2.2	
14	5101-13-3	Pyrite	−1.02		33	5101-11	Pyrite	−0.5	
15	5101-10-2	Pyrite	−1.14		34	5101-11(2)	Pyrite	−0.1	
16	5101-10-3	Pyrite	−0.48		35	5101-12	Pyrite	−1.4	
17	5101-14-1	Pyrite	0.50		36	5101-13	Pyrite	−0.5	
18	5101-7B-1	Sphalerite	−2.01		37	5101-21	Pyrite	−0.1	
19	5101-7B-2	Sphalerite	−3.11		38	5101-22	Pyrite	−1.2	

Table 5
Lead isotope compositions of sulfides and rocks from the Huangtan deposit.

No.	Sample	Mineral or rock	$^{208}Pb/^{204}Pb$	Std err	$^{207}Pb/^{204}Pb$	Std err	$^{206}Pb/^{204}Pb$	Std err
1	5101-6	Pyrite	37.619	0.005	15.499	0.002	18.456	0.003
2	5101-10	Pyrite	37.350	0.004	15.448	0.002	17.868	0.002
3	5101-11	Pyrite	37.376	0.003	15.457	0.002	17.877	0.002
4	5101-11(2)	Chalcopyrite	37.397	0.005	15.460	0.002	17.886	0.002
5	5101-12	Pyrite	37.456	0.004	15.465	0.002	17.909	0.002
6	5101-13	Chalcopyrite	37.351	0.003	15.446	0.001	17.878	0.001
7	5101-21	Pyrite	37.539	0.008	15.492	0.003	17.921	0.003
8	TC4300-9	Quartz diorite	38.491	0.002	15.567	0.001	19.495	0.001
9	TC4400-11	Quartz diorite	38.267	0.002	15.552	0.001	19.231	0.001
10	4301-3	Quartz diorite	38.271	0.002	15.548	0.001	19.220	0.001
11	4401-2	Basalt	38.043	0.001	15.536	0.000	18.332	0.000
12	TC4400-8	Andesite	38.243	0.001	15.554	0.001	18.205	0.001
13	TC4400-1	Dacitic tuff	38.466	0.001	15.575	0.001	19.375	0.001

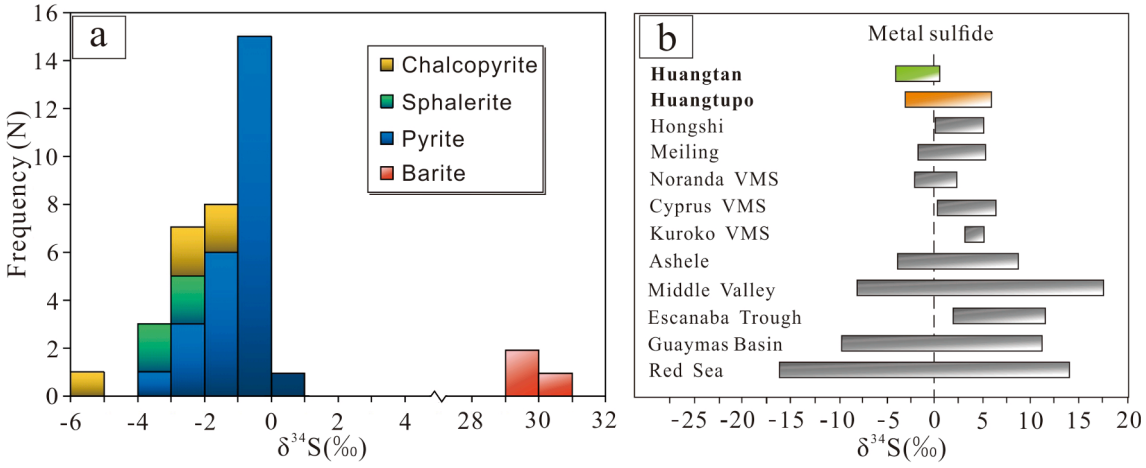

Fig. 14. a: Histogram of sulfur isotope compositions for various sulfides from the Huangtan deposit; b: a comparison with $\delta^{34}S$ values of sulfide minerals in typical VMS deposits worldwide (modified from Dai et al., 2004).

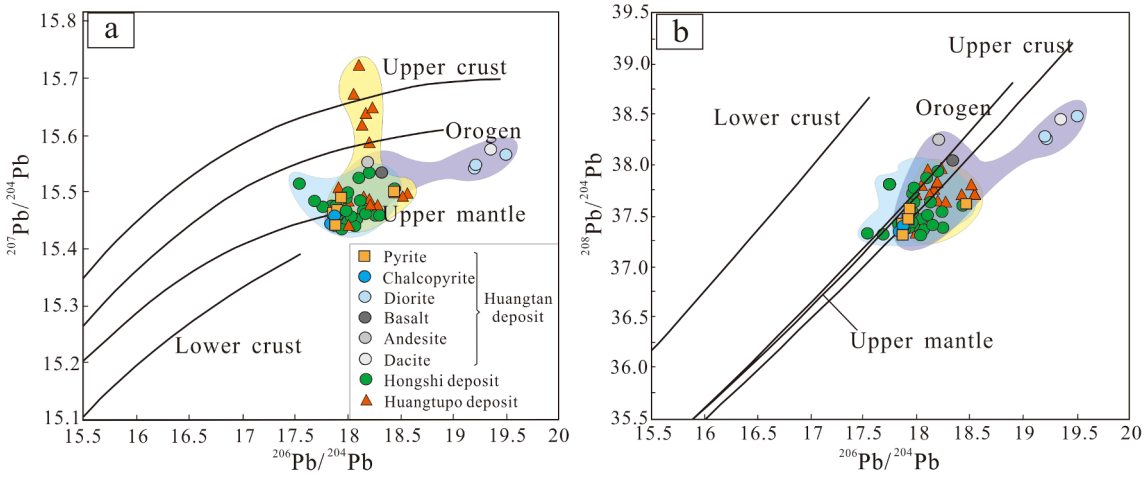

Fig. 15. Lead isotopic compositions of sulfides and host rocks from the Huangtan deposit. a: $^{207}Pb/^{204}Pb$ vs. $^{206}Pb/^{204}Pb$; b: $^{208}Pb/^{204}Pb$ vs. $^{206}Pb/^{204}Pb$ (Pb isotopic data of the Huangtupo and Hongshi deposits were obtained from Mao et al., 2019; Deng et al., 2020). The evolution curves of the upper crust, lower crust, mantle and orogen are from Zartman and Doe (1981).

Huangtan deposit and peripheral altered pyroclastic rocks have simultaneously experienced regional compression deformation and fragmentation. This ^{40}Ar-^{39}Ar plateau age may also represent the age of regional tectonic activity. Similar tectonic deformation events have been observed in the adjacent Huangtupo deposit (Mao et al., 2019).

6.2. *The nature of the ore-forming fluids*

FIs of the Huangtan Au-Cu deposit are dominated by liquid-rich (L-type) two-phase inclusions, suggesting a relatively simple salt-water system and similar to most VMS deposits, which are characterized by low salinity and limited CO_2-dominant inclusions (Luders et al., 2001;

Zaw et al., 2003). Petrographic observations and statistics show that there is a certain pattern of variation in fluid inclusion types and peak homogeneous temperatures from deep to shallow (Fig. 16). Primary FIs in the hydrothermal channel vein-disseminated ores have higher homogenization temperatures (230 to 380 °C, peak 310 °C) than those of FIs in the shallow exhalative-sedimentary layered-massive ores (170 to 300 °C, peak 240 °C). The petrographic and microthermometric studies of primary FIs hosted in quartz and barite from S1 to S3 display a gradual decrease of temperature, i.e., the homogenization temperatures range from 379 °C to 118 °C (Table 2, Fig. 11 and Fig. 13a). Fluid salinity shows a similar decreasing trend, i.e., from 14.2 to 0.3 wt% NaCl equiv, indicating fluid mixing or dilution. The homogenization temperature and salinity ranges are consistent with most Au-rich and auriferous VMS-type deposits (Mercier-Langevin et al., 2011).

The peak temperature interval of FIs in the S1 ranges from 300 °C to 310 °C, showing the characteristic of a medium temperature fluid, i.e., typical features of intermediate-density, VMS-type FIs (Luders et al., 2001). Widespread chlorite formation around the orebodies evidences a rapid temperature decrease at this stage, with temperatures of 255 ± 50 °C (Zang and Fyfe, 1995). Halite-bearing inclusion was rarely identified in the S1 hydrothermal quartz, except for several sulfate-bearing inclusion (Fig. 10g). Pyrite-bearing S-type FIs have been frequently observed, which means that local high-salinity and high ore-bearing fluid activity in initial ore-forming fluids during the early ore stage (Fig. 10f). Some low-salinity L- and V-types FIs coexist and have similar homogenization temperatures (Table 2; Fig. 10e), suggesting the existence of local fluid immiscible or boiling (Hedenquist et al., 1998; Simmons et al., 2005). Fluid immiscibility results in an obvious loss of volatiles such as N_2, CH_4, and CO_2, but no liquid CO_2 -bearing three-phase inclusions were found throughout the evolution process (Hedenquist et al., 1998; Simmons et al., 2005). FIs of the same type with opposing homogenization characteristics (to liquid and vapor) at similar temperatures provide further evidence for local fluid boiling. For example, co-existing L-, and V-type FIs are homogenized to liquid and vapor at temperatures of 305–319 °C, which indicates boiling (Cheng et al., 2020). This situation will promote the occurrence of water–rock reaction and aggravate hydrothermal alteration.

The decreasing temperatures and salinities of fluids, and abundance of barite during S2 could reflect an incursion of an external fluid (Fig. 5g, Fig. 10h and Fig. 11). We speculate that the mixing of ancient seawater and magmatic water in the main metallogenic stage (S2) may be a crucial factor of mineral precipitation. The FIs found in the quartz and calcite from S3 are characterized by low homogenization temperatures (118–198 °C) and low salinities (0.3–14.1 wt% NaCl equiv), which represent the waning and coolest stage of this hydrothermal evolution system and the end of mineralization (Fig. 11e, f). Mixing with seawater results in increased hydrothermal fluid density and local salinity (Fig. 13a). Ore-forming fluids at this stage belongs to a typical H_2O–NaCl system.

In addition, laser Raman analyses indicate that the CO_2, CH_4 and N_2 contents from S1 to S3 tend to decrease gradually. The ore fluid evolved can be described from an early H_2O-NaCl ± CO_2 ± CH_4 system to a late NaCl-H_2O system with mineralizing fluid diluted and reduced. We conclude that mineral (Cu-Zn-Au sulfides) precipitation from ore fluids is mainly due to P-T and pH change as the hydrothermal fluids upwelling and mix with cold, ambient seawater.

6.3. Source of ore-forming fluids and materials

6.3.1. Sources of the ore-forming fluids

The quartz samples from the S1 quartz veins show relatively high $\delta^{18}O_{H2O}$ (1.7 to 5.6‰) and $\delta D_{V\text{-}SMOW}$ (-60.2 to −66.8‰) values, consistent with those reported in other VMS metallogenic deposits (e.g., Huangtupo deposit; Cheng et al., 2020; Huston, 1999), indicating a magmatic fluid dominated signature (Fig. 13b; Sheppard and Gustafson, 1976; Taylor et al., 1974; Taylor and Sheppard, 1986). The samples from the S2 and S3 show relatively lower $\delta^{18}O_{H2O}$ (−6.1 to −0.2‰) and $\delta D_{V\text{-}SMOW}$ (−58.4 to −53.9‰) values than those from S1 veins. All samples are plotted out of the primary magmatic water box region and extended towards the meteoric water line and SMOW zone, indicating that large amounts of seawater were involved in mineralization (Fig. 13b). The mixing of seawater may be a major factor for the lower values of $\delta^{18}O_{H2O}$ than magmatic fluid. This process happened predominantly in the higher permeability areas near the seafloor where discrete circulation cells are formed and seawater recharge is enhanced (Hannington et al., 2005). Besides, studies have shown that elemental sulfur and acid can be produced by oxidation and hydrolysis reactions when sulfur gases mix with seawater (e.g., Giggenbach, 1996; de Ronde, 2005). Some advanced argillic mineral assemblages of silica polymorphs + native sulfur + alunite + pyrite ± kaolinite were found at Huangtan, especially at the channel site (Fig. 6b), which further evidence for the presence of magma fluid mixed with seawater (de Ronde, 2005). These features

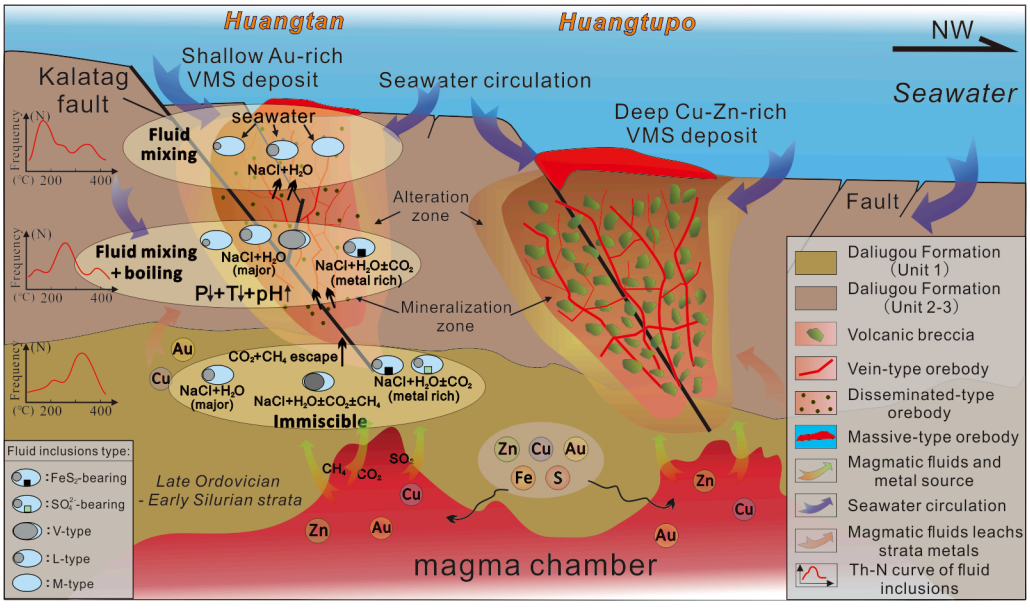

Fig. 16. Schematic illustration showing the genetic model for the Huangtupo-Huangtan deposit.

Table 6
Geological characteristics of Huangtan and Huangtupo deposits in the Kalatag district, Eastern Tianshan.

Deposits	Longitude, latitude	Type	Metals	Reserve@ ore grade	Host rocks	Ore-controlling structure	Intrusion	Mineragenetic epoch	Occurrence of orebody	Major alteration	Ore mineral	Gangue mineral	Reference
Huangtan	91°56′ 05″ E, 42°34′08″N	VMS	Au-Cu-Zn	Au: 5 t@>1g/t; Cu:10Kt@0.3%; Zn: 100Kt@1.5%	Ordovician–Silurian volcanic rocks (O_d)	NW-trending faults	Quartz diorite, Rhyolite porphyry	Early Silurian (4370 ± 6Ma)	Stratoid Cu-Zn orebody and lenticular Au orebody	Silicification, pyritization, sericitization, phyllic alteration, carbonate	Pyrite + chalcopyrite + sphalerite + galena	Quartz + sericite + barite + carbonate	Deng et al., 2020; Sun et al., 2020
Huangtupo –(Honghai)	91°55′40″ E, 42°36′ 39″N	VMS	Cu-Zn-(Au-Ag-Ga-Cd)	Cu:300Kt@1.49%; Zn:280Kt@3.51%; Au:7.1 t@0.6 g/t; Ag:281 t@26 g/t; Ga:278 t@12.9 g/t; Cd:372 t@17.3 g/t	Ordovician–Silurian volcanic sedimentary rocks (O_d)	NW-trending faults and contact zone between the felsic lava and tuff	Quartz diorite, granite, and granite porphyry	Early Silurian (434 ± 4Ma)	Massive Cu-Zn orebody and vein type Cu orebody	Phyllic alteration, pyritization, chloritization, epidotization, albitization, carbonate	Pyrite + chalcopyrite + sphalerite + galena + tetrahedrite + pyrrhotite	Quartz + sericite + barite + chlorite + carbonate + plagioclase	Deng et al., 2016a,b

were similar to other contemporaneous deposits in this area (i.e., those deposits showed $\delta D_{V\text{-}SMOW}$ values from −136 to −36‰ and $\delta^{18}O_{H2O}$ values from −5.8 to 5.9‰; Fig. 13b; Deng et al., 2020). This could mean that the Huangtan deposit formed near a magmatic-hydrothermal channel and ore-forming fluids were derived mainly from magmatic fluids mixed with deep-circulation seawater.

6.3.2. Sources of sulfur and metals

In general, the sulfur enrichment with $\delta^{34}S$ values ranging from −5 to +5‰ in VMS deposits is commonly interpreted to have a magmatic sulfur origin (Franklin et al., 2005). The $\delta^{34}S$ values of sulfides in the Huangtan Au-Cu deposit have a limited range from −5.25 to 0.50‰ (average = −1.44‰, n = 35), and are similar to but slightly more negative than those of sulfides from the majority of magmatic-hydrothermal deposits (−3 to +1‰; Hoefs, 2009). These $\delta^{34}S$ data tend to shift toward more negative values with progressive precipitation of sulfide minerals. The lack of large volumes of terrigenous sediment at Kalatag district suggests that negative $\delta^{34}S$ values are not due to the biogenic reduction of seawater sulfur, although local bacterial activity in the hydrothermal plume may have had a limited effect on a seawater sulfate source. We believe the negative $\delta^{34}S$ values are mainly related to the disproportionation of SO_2 and may be inherited from the magmatic source by the following reaction: $3SO_2 + 3H_2O = S^0 + 2H^+ + 2HSO_4^-$, $4SO_2 + 4H_2O = H_2S + 3H^+ + 3HSO_4^-$ or $2H_2S + SO_2 \rightarrow 2H_2O + 3S^0$ (Gamo et al., 1997; Hannington et al., 2005; de Ronde, 2005; de Ronde et al., 2011). This means that acid and sulfate can be largely generated in volcanoes discharging high concentrations of magmatic volatiles (Massoth et al., 2003). The presence of sulphate minerals in FIs and alteration ranges also confirms the occurrence of this process (Fig. 6b, i and Fig. 9g).

Besides, the Pb isotope ratios of the seven sulfide samples were similar and showed well comparability with the values of associated igneous rocks (Fig. 15a, b). The majority of Pb isotopic compositions of the Huangtan sulfides plot in the field between the upper mantel and crust, reflecting mixed mantle and upper crustal sources (Table 4; Fig. 15). The Early Paleozoic magmatism may have contributed most of the lead and ore-forming metals (Sun et al., 2020). This result coincides well with the deficiency of Cu and Zn metallogenic elements in altered footwall volcanic rocks. Moreover, Sr-Nd isotope analyses of volcanic rocks in the Huangtan deposit have relatively homogeneous Nd isotopic compositions of $\varepsilon_{Nd}(t) = 5.3$ to 7.2 and are in close agreement with the isotopic data of corresponding sulfides (Sun et al., 2020). The magmatic fluids, therefore, may contribute significant amounts of sulfur and potentially appreciable metallic components. Some fluid-inclusion evidence indicates that magmatic vapors can carry exceptionally high metal contents (Williams-Jones and Heinrich, 2005), thus raising the possibility that a short-term, limited-volume, magmatic flux could be very important in providing metals to the system. We also found FIs containing metallic mineral crystals in the quartz of the early and main-stage (S1-2; Fig. 10a, f), which indirectly proves this point.

To summarize, the initial, hottest ore-forming fluids were predominantly derived from Early Paleozoic magmas and underwent a varying degree of mixing with seawater. The ore-forming materials were mainly derived from the upper mantle with a minor contribution of crust.

6.4. Ore genesis of the Huangtan deposit

It is well documented that the Cu-Au mineralization of the Kalatag orefield is closely associated with the Early Silurian intra-ocean arc rifting environment during the northward subduction of the oceanic lithosphere (Chai et al., 2019; Sun et al., 2020). Several ancient calderas (Yudai, Hongshan, Meiling, Hongshi, and Honghai) developed at this period, accompanied by a series of NW- and NNW-striking faults (Mao et al., 2019). These structures constitute important ore-controlling and ore-hosting structures in the Kalatag district. For example, some outward-dipping faults around the calderas are identified as critical

transport pathways for seawater and geothermal fluids. The known Huangtupo, Hongshi, Meiling, and other deposits are obviously controlled by these structures (Fig. 2). As a newly discovered deposit, the Huangtan deposit shows similar geological and geochemical features to the adjacent Huangtupo VMS Cu-Zn deposit (Sun et al., 2020; Deng et al., 2020). They have the same metallogenic tectonic setting, similar metallogenic epoch and assemblage of elements, minerals and rocks (Table 6; Mao et al., 2019; Sun et al., 2020). After comprehensive consideration, the possibility that Huangtan deposit belongs to other types of deposits is excluded. The comparison of geological characteristics of the two deposits is summarized in Table 6 and graphically illustrated in Fig. 16. Similar origins of their ore-forming materials and fluids are also illustrated by the S-Pb-H-O isotopic compositions (Fig. 13b, Fig. 14, and Fig. 15). One obvious difference is that the Huangtupo deposit is rich in copper and zinc, while the Huangtan deposit is relatively rich in gold and copper. Moreover, the main ore stage of Huangtupo has hydrostatic pressure of 13–17 MPa and depth of > 1000 m (Gao, 2013), while that of the Huangtan deposit (S3) has a lower metallogenic pressure (<10 MPa) and shallower depth (<1000 m). In general, VMS deposits are clustered, and some VMS deposits associated with caldera-forming faults usually have similar ore-forming element differences with Huangtupo-Huangtan deposits (Stix et al., 2003; Martin et al., 2021). The VMS deposits rich in Zn and Cu usually occurred in the deeper water environment at the core of a subsidence structure, while the VMS deposits rich in Au-Cu may be formed in the shallow water environment along the margin of the subsidence structure (Kerr and Gibson, 1993). This situation can be explained as that the ore-forming fluid emanating from faults at structurally higher levels are subjected to greater boiling at shallower water depths, which is conducive to gold precipitation and enrichment (Stix et al., 2003). Similar instances developed in the Noranda, Canada, and is consistent with the VMS metallogenic system of Huangtan-Huangtupo (Kerr and Gibson, 1993; Gibson and Watkinson, 1990). In addition, black smoke vents in modern seafloor hydrothermal systems develop only in the high-temperature portion of the system with extinct sulfide accumulations preserved distally. At the margin of the sulfide mound, white chimneys usually form and release lower-temperature fluids, which is more Au-rich than black chimneys (Webber et al. 2017; Martin et al., 2021). Such a hydrothermal system may also have occurred in the Early Paleozoic Kalatag district. The Huangtan deposit may be a distal adjunct of the Huangtupo submarine hydrothermal system, and there may be potential undiscovered similar deposits in the Kalatag district.

In our opinion, the subvolcanic intrusions in the field are considered to be a heat source to drive the hydrothermal convective system and a potential direct source of some metals. Under immiscibility, magmatic fluids overflowed and carried metallogenic material invaded the fractures in the Daliugou Formation. Gold in the bottom surrounding rock was initially mobilized during high-temperature (>350 °C) fluid-rock interaction, that form a source region for some metals (Mao et al. 2019). The negative pH and positive Al anomalies in hydrothermal plumes are considered to reflect volcanic degassing of CO_2 and SO_2 (Gamo et al., 1997; Hannington et al., 2005). Widespread muscovite and potash feldspar in Cu-polymetallic veins provide direct evidence of venting of volcanic-derived sulfur gases (Fig. 5n). The ore-forming fluid heated by deep magma chambers rises along the caldera faults at decreasing temperature and pressure, leading to local boiling and producing an ore-forming H_2O-NaCl ± CO_2 ± CH_4 hydrothermal fluid system (Stix et al., 2003). In addition, the peripheral parts of the fluid system further interacted with the surrounding rocks, accompanied by leaching and enrichment of metallogenic metals, such as Cu, Zn, Au, and Fe, in the stratum. Cold ambient seawater flowed downward through peripheral faults, and mixed with magmatic fluids within the transitional zone, which facilitates the precipitation of secondary pyrite that incorporates trace metals. Some veined and disseminated mineralization occurred mainly at, or within close proximity to the spreading axis at this stage (<250 °C). In the shallow low-temperature alteration zone, an increase in seawater entrainment further cools and dilutes the hydrothermal system, which is shown by the assemblage smectite + chlorite + barite + pyrite and/or hematite + goethite + zeolites (Fig. 6a, b). These changes forced the pH increase and the oxygen fugacity change, consequently reducing the stability of metallic particles (Franklin et al., 2005; Voute et al., 2019) and leading to precipitation of major sulfides in the feeder zone near a caldera. The ore-forming mechanism model is schematically shown in Fig. 16. This genetic model we proposed to account for the spatial distribution of the VMS-type Cu-Au-Zn mineralization can be used for prospecting. The peripheral and distal area around Huangtan-Huangtupo mineralization has potential for more VMS deposits. Regionally, the Early Paleozoic caldera structure should be further identified for exploration of VMS Cu-polymetallic deposits.

7. Conclusions

1. The muscovite sample found at the late ore stage (S3) coexisting with pyritic phyllic alteration has a ^{40}Ar-^{39}Ar plateau age of 414.4 ± 0.4 Ma, which represents the upper age limit of shallow hydrothermal alteration and Au-Cu mineralization.
2. Sulfur and lead isotope composition of sulfides imply that the ore-forming materials were mainly derived from the upper mantle with a minor contribution of crust in the Huangtan deposit. Microthermometry, $\delta^{18}O_{H2O}$ and $\delta D_{V\text{-}SONW}$ values for the FIs constrain that the ore-forming fluids are characterized by low-medium temperatures and low salinities, consisting of magmatic fluids that mixed with seawater fluids. The FIs define an H_2O-NaCl ± CO_2 ± CH_4-bearing hydrothermal evolutionary system.
3. The presence of CO_2-bearing FIs coexisting with liquid- and vapor-rich inclusions in the S1 quartz veins suggests that fluid phase separation occurred at the early mineralization. The precipitation of sulfide and gold was mainly controlled by the rapid temperature drop and pH rise due to the mixing of magmatic fluid with seawater. Fluid mixing and local boiling can promote hydrothermal alteration and mineralization.
4. The Huangtan deposit may be a distal product of the adjacent Huangtupo VMS deposit. These two VMS deposits constitute a unique VMS metallogenic system, which provides an important research object for ore prospecting in the peripheral Gobi Desert area.

Declaration of Competing Interest

The authors declare that they have no known competing financial interests or personal relationships that could have appeared to influence the work reported in this paper.

Acknowledgements

This study is financially supported by the National Natural Science Foundation of China (grant 41802101), the China Geologic Survey Program (grants DD20179607), the Basic University Research Fund from Ministry of Education of China (grants G1323541879 and G1323541839). We sincerely thank the staff of the Xinjiang Xituo Mining Limited Liability Company for their gracious support of our fieldwork. We are also appreciative of Yuan Zhang, Wei Wei and Xuewen Pan for their help to prepare samples for analysis. Finally, we are also grateful to the laboratory teachers and technicians in helping us achieve the research goals for this study and the two anonymous reviewers for their constructive and valuable comments.

References

Baker, J., Peate, D., Waight, T., Meyzen, C., 2004. Pb isotopic analysis of standards and samples using a ^{207}Pb–^{204}Pb double spike and thallium to correct for mass bias with a double-focusing mc-icp-ms. Chem. Geol. 211 (3–4), 275–303.

Bodnar, R.J., 1993. Revised equation and table for determining the freezing point depression of H_2O–NaCl solutions. Geochim. Cosmochim. Acta 57, 683–684.
Burke, E.A., 2001. Raman microspectrometry of fluid inclusions. Lithos 55, 139–158.
Chai, F.M., Zhang, Z.C., Li, W.H., Santosh, M., Wang, H.P., Wang, W., Xu, Q.F., 2019. The early Paleozoic Huangtupo VMS Cu-Zn deposit in Kalatag, Eastern Tianshan: Implications from geochemistry and zircon U-Pb geochronology of volcanic host rocks. Lithos 342–343, 97–113.
Chen, L., Wang, J.B., Bagas, L., Wu, X.B., Zou, H.Y., Zhang, H.Q., Sun, Y., Lv, X.Q., Deng, X.H., 2017. Significance of adakites in petrogenesis of early Silurian magmatism at the Yudai copper deposit in the Kalatag district, NW China. Ore Geol. Rev. 91, 780–794.
Chen, Y.J., Pirajno, F., Wu, G., Qi, J.P., Xiong, X.L., 2012. Epithermal deposits in North Xinjiang, NW China. Int. J. Earth Sci. 101, 889–917.
Cheng, X.H., Yang, F.Q., Zhang, R., Xu, Q.F., Li, N., 2020. Metallogenesis and fluid evolution of the Huangtupo Cu–Zn deposit, East Tianshan, Xinjiang, NW China: Constraints from ore geology, fluid inclusion geochemistry, H-O-S isotopes, and U-Pb zircon, Re-Os chalcopyrite geochronology. Ore Geol. Rev. 121, 103469.
Claypool, G.E., Holser, W.T., Kaplan, I.R., Sakai, H., Zak, I., 1980. The age curves of sulfur and oxygen isotopes in marine sulfate and their mutual interpretation. Chem. Geol. 28, 3–4.
Clayton, R.N., O'Neil, J.R., Mayeda, T.K., 1972. Oxygen isotope exchange between quartz and water. J. Geophys. Res. 77, 3057–3067.
Dalrymple, G.B., Lanphere, M.A., 1969. In: Potassium-argon Dating—Principles, Techniques, and Applications to Geochronology. Freeman, San Francisco, W.H, p. 258.
Dai, B.Z., Zhao, K.D., Jiang, S.Y., 2004. Progress in the study of modern submarine hydrothermal activity and genesis of massive sulfide deposits. Bull. Mineral. Petrol. Geochem. 23, 246–253.
Deng, X.H., Wang, J.B., Pirajno, F., Wang, Y.W., Li, Y.C., Li, C., Zhou, L.M., Chen, Y.J., 2016a. Re–Os dating of chalcopyrite from selected mineral deposits in the Kalatag district in the Eastern Tianshan Orogen, China. Ore Geol. Rev. 77, 72–81.
Deng, X.H., Wang, J.B., Santosh, M., Li, Y.C., Wang, Y.W., Mao, Q.G., Long, L.L., Chen, X., 2016b. New $^{40}Ar/^{39}Ar$ ages from the Kalatag district in the Eastern Tianshan, NW China: constraints on the timing of Cu mineralization and stratigraphy. Ore Geol. Rev. 100, 250–262.
Deng, X.H., Li, Y.C., Xu, Q.F., Liu, Y., Zhang, R., Li, D.D., X, F., 2018. Discovery and significance of the Jinling-Huangtan gold - copper deposit in the Kalatag district, Eastern Tianshan, NW China. Mineral Exploration 9 (07), 1322–1333 (in Chinese).
Deng, X.H., Wang, J.B., Franco, P., Mao, Q.G., Long, L.L., 2020. A review of Cu-dominant mineral systems in the Kalatag district, East Tianshan, China. Ore Geol. Rev. 117, 103284.
de Ronde, C.E.J., 2005. Evolution of a Submarine Magmatic-Hydrothermal System: Brothers Volcano, Southern Kermadec Arc, New Zealand. Econ. Geol. Bull. Soc. Econ. Geol. 100, 1097–1133.
de Ronde, et al., 2011. Submarine hydrothermal activity and gold-rich mineralization at Brothers volcano, Kermadec arc, New Zealand. Mineral. Deposita 46, 541–584.
Dubé, B., Gosselin, P., Mercier-Langevin, P., Hannington, M., and Galley,A., 2007. Gold-rich volcanogenic massive sulphide deposits: Geological Association of Canada, Mineral Deposits Division, Special Publication no. 5, pp. 75-94.
Franklin, J.M., Lydon, J.W., Sangster, D.F., 1981. Volcanic-associated massive sulfide deposits. In: Skinner, B.J. (Ed.), Economic Geology Seventy-fifth Anniversary Volume 1905-1980, pp. 485–627.
Franklin, J.M., Gibson, H.L., Jonasson, I.R., Galley, A.G., 2005. Volcanogenic massive sulfide deposits. Econ. Geol. 100th Anniversary Volume 98, pp. 523–560.
Gamo, T., et al., 1997. Acidic and sulfate-rich hydrothermal fluids from the Manus back-arc basin, Papua New Guinea. Geol. (Boulder) 25 (2), 139–142.
Gao, Q., 2013. The Research on Geological Characteristics and Metallogenic Analysis of Huangtupo Copper-Zinc Deposit in Kalatag Area, East Tianshan Mountain, Xinjiang Prov. Master thesis. China University of Geosciences (Wuhan), pp. 1–74 (in Chinese with English abstract).
Gibson, H.L., and Watkinson, D.H., 1990, Volcanogenic massive sulfide deposits of the Noranda cauldron and shield volcano, Quebec. In Rive, M.,et al., eds., The northwestern Quebec polymetallic belt: A summary of 60 yr of mining exploration: Canadian Institute of Mining and Metallurgy Special Volume 43, pp. 119–132.
Giggenbach, W.F., 1996. Chemical composition of volcanic gases. In: Tilling, R.I., Scarpa, R. (Eds.), Monitoring and mitigation of volcano hazards: Berlin. Springer-Verlag, pp. 221–256.
Goldfarb, R.J., Groves, D.I., Gardoll, S., 2001. Orogenic gold and geologic time: a global synthesis. Ore Geol. Rev. 18, 1–75.
Goldfarb, R.J., Taylor, R.D., Collins, G.S., Goryachev, N.A., Orlandini, O.F., 2014. Phanerozoic continental growth and gold metallogeny of Asia. Gondwana Res. 25, 48–102.
Hannington, M.D., deRonde, C.E.J., Petersen, S., 2005. Seafloor tectonics and submarine hydrothermal systems. Econ. Geol. 111–141.
Hedenquist, J.W., Arribas, A., Reynolds, T.J., 1998. Evolution of an intrusion-centere hydrothermal system; Far Southeast-Lepanto porphyry and epithermal Cu-Au deposits, Philippines. Econ. Geol. 93, 373–404.
He, X.H., 2019. Metallogenesis of Huangtan Au-Cu deposit in Kalatag ore Concentration Area, East Tianshan. Master thesis. China University of Geosciences (Beijing), pp. 1–55 (in Chinese with English abstract).
Hoefs, J., 2009. In: Stable Isotope Geochemistry, sixth ed. Springer-Verlag, Berlin, Heidelberg, p. 285.
Hokka, J., 2020. Geology, alteration and lithogeochemistry of the Paleoproterozoic Korpela VMS occurrence in Eastern Finland. Minera. Deposita 55 (8), 1581–1604.
Huang, X.W., Qi, L., Gao, J.F., Zhou, M.F., 2013. First reliable Re-Os ages of pyrite and stable isotope compositions of Fe(-Cu) deposits in the Hami region, eastern Tianshan orogenic belt, NW China. Resour. Geol. 63, 166–187.
Huston, D.L., 1999. Stable isotopes and their significance for understanding the genesis of volcanic-hosted massive sulfide deposits—a review. In: Barrie, C.T., Hannington, M.D. (Eds.), Volcanic-associated massive sulfide deposits—Processes and examples in modern and ancient settings: Reviews in Economic Geology, pp. 157–179.
Huston, D.L., 2000. Gold in volcanic-hosted massive sulfide deposits: Distribution, genesis, and exploration. Rev. Econ. Geol. 13, 401–426.
Kerr, D.J., Gibson, H.L., 1993. A comparison of the Horne volcanogenic massive sulfide deposit and intracauldron deposits of the Mine Sequence, Noranda. Quebec: Econ. Geol. 88, 1419–1442.
Liang, B., 2018. Geological characteristics and genesis analysis of Gold and copper polymetallic deposit in Huangtan, Hami, Xinjiang Province. Xinjiang Nonferrous Met. 2, 62–65 (in Chinese).
Li, S., Wang, T., Wilde, S.A., Tong, Y., 2013. Evolution, source and tectonic significance of early Mesozoic granitoid magmatism in the Central Asian Orogenic Belt (central segment). Earth Sci. Rev. 126, 206–234.
Liu, D.Q., Chen, Y.C., Wang, D.H., Tang, Y.L., Zhou, R.H., Wang, J.L., Li, H.Q., Chen, F. W., 2003. A discussion on problem related to mineralization of Tuwu-Yandong Cu-Mo orefield in Hami, Xinjiag. Miner. Deposit 22, 334–344 (in Chinese with English abstract).
Luders, V., Pracejus, B., Halbach, P., 2001. Fluid inclusion and sulfur isotope studies in probable modern analogue Kuroko-type ores from the JADE Hydrothermal field (Central Okinawa trough, Japan). Chem. Geol. 173, 45–58.
Mao, Q.G., Wang, J.B., Fang, T.H., Zhu, J.J., Fu, W.W., Yu, M.J., Huang, X.K., 2015a. Lead and sulfur isotope studies of sulfides from Honghai VMS-type deposit in Kalatage ore belt of eastern Tianshan Mountains. Miner. Deposits 34 (04), 730–744.
Mao, Q.G., Yu, M.J., Xiao, W.J., Windley, B.F., Li, Y.C., Wei, X.F., Zhu, J.J., Lu, X.Q., 2018. Skarn-mineralized porphyry adakites in the Harlik arc at Kalatage, E. Tianshan (NW China): Slab melting in the Devonian-early Carboniferous in the southern Central Asian Orogenic Belt. J. Asian Earth Sci. 153, 365–378.
Mao, Q.G., Wang, J.B., Xiao, W.J., Brian, F., Karel, S., Yu, M.J., Fang, T.H., Li, Y.C., 2019. Mineralization of an intra-oceanic arc in an accretionary orogen: insights from the Early Silurian Honghai volcanogenic massive sulfide Cu-Zn deposit and associated adakites of the Eastern Tianshan (NW China). GSA Bull. 131 (5–6), 803–830.
Mao, Y.J., Qin, K.Z., Li, C.S., Tang, D.M., 2015b. A modified genetic model for the Huangshandong magmatic sulfide deposit in the central Asian Orogenic Belt, Xinjiang, western China. Miner. Deposita. 50, 65–82.
Martin, A.J., McDonald, I., McFall, K.A., 2021. Low-temperature silica-rich gold mineralization in mafic VMS systems: evidence from the Troodos ophiolite, Cyprus. Miner Deposita. 56, 805–822.
Massoth, G.J., de Ronde, C.E.J., Lupton, J.E., Feely, R.A., Baker, E.T., Lebon, G.T., Maenner, S.M., 2003. Chemically rich and diverse submarine hydrothermal plumes of the southern Kermadec volcanic arc (New Zealand). In: ., vol. 219, pp. 119–139.
Mercier-Langevin, P., Hannington, M.D., Dubé, B., Bécu, V., 2011. The gold content of volcanogenic massive sulfide deposits. Mineral. Deposita 46, 509–539.
Ohmoto, H., Mizukami, M., Drummond, S.E., Eldridge, C.S., Pisutha-Arnond, V., Lenaugh, T.C., 1983. Chemical processes in kuroko formation. Econ. Geol. Monogr. 5, 570–604.
Renne, P.R., Swisher, C.C., Deino, A.L., Karner, D.B., Owens, T.L., DePaolo, D.J., 1998. Intercalibration of standards, absolute ages and uncertainties in $^{40}Ar/^{39}Ar$ dating. Chem. Geol. 145, 117–152.
Pilote, J., Piercey, S.J., Mercier-Langevin, P., 2020. Evolution of the subseafloor hydrothermal system associated with the Ming VMS deposit, Newfoundland Appalachians, and its controls on base and precious metal distribution. Mineral. Deposita 55, 913–936.
Pirajno, F., Seltmann, R., Yang, Y.Q., 2011. A review of mineral systems and associated tectonic settings of northern Xinjiang, NW China. Geosci. Front. 2, 157–185.
Pirajno, F., 2013. In: The Geology and Tectonic Settings of China's Mineral Deposits. Springer, Berlin, pp. 1–671.
Poulsen, K.H., Hannington, M.D., 1996. Volcanic-associated massive sulphide gold: Ottawa, ON, Geological Survey of Canada. Geol. Canada Ser. 8, 183–196.
Roedder, E., 1984. Fluid inclusions. Rev. Mineral. 12, 646.
Şengör, A.M.C., Natal'in, B.A., Burtman, V.S., 1993. Evolution of the Altaid tectonic collage and Palaeozoic crustal growth in Eurasia. Nature 364, 299–307.
Shen, P., Pan, H.D., Zhou, T.F., Wang, J.B., 2014. Petrography, geochemistry and geochronology of the host porphyries and associated alteration at the Tuwu Cu deposit, NW China: a case for increased depositional efficiency by reaction with mafic hostrock? Mineral. Deposita 49, 709–731.
Sheppard, S.M.F., Gustafson, L.B., 1976. Oxygen and hydrogen isotopes in the porphyry copper deposit at El Salvador, Chile. Econ. Geol. 71, 1549–1559.
Simmons, S.F., White, N.C., John, D., 2005. Geological characteristics of epithermal precious and base metal deposits. Economic Geology100th Aniversary Volume, pp. 485–522.
Stix, J., Kennedy, B., Hannington, M., Gibson, H., Fiske, R., Mueller, W., Franklin, J., 2003. Caldera-forming processes and the origin of submarine volcanogenic massive sulfide deposits. Geology (Boulder). 31 (4), 375.
Sun, Y., Wang, J.B., Wang, Y.W., Long, L.L., Mao, Q.G., Yu, M.J., 2019a. Ages and origins of granitoids from the Kalatag Cu cluster in Eastern Tianshan, NW China: constraints on Ordovician-Devonian arc evolution and porphyry Cu fertility in the Southern Central Asian orogenic belt. Lithos 330–331, 55–73.
Sun, Y., Wang, J.B., Lv, X.Q., Yu, M.J., Li, Y.C., Mao, Q.G., Wang, Y.W., Long, L.L., 2019b. Geochronology, petrogenesis and tectonic implications of the newly

discovered Cu–Ni sulfide-mineralized Yueyawan gabbroic complex, Kalatag district, northwestern Eastern Tianshan, NW China. Ore Geol. Rev. 109, 598–614.
Sun, B.K., Ruan, B.X., Lv, X.B., Bieersen, T., Michael, E.R., 2020. Geochronology and geochemistry of the igneous rocks and ore-forming age in the Huangtan Au Cu deposit in the Kalatag district, Eastern Tianshan, NW China: Implications for petrogenesis, geodynamic setting, and mineralization. Lithos 368–369, 105594.
Taylor, H.P., 1974. The application of oxygen and hydrogen isotope studies to problems of hydrothermal alteration and ore deposition. Econ. Geol. 69, 843–883.
Taylor, H.P., Sheppard, S.M.F., 1986. Igneous rocks: 1. Processes of isotopic fractionation and isotope systematics. Rev. Mineral. Geochem. 16, 227–271.
Vasconcelos, P., 1999. $^{40}Ar/^{39}Ar$ geochronology of supergene processes in ore deposits. In: Lambert, D.D., Ruiz, J. (Eds.), Application of Radiogenic Isotopes to Ore Deposit Research and Exploration. Society of Economic Geologists, Littleton, pp. 73–113.
Voute, F., Hagemann, S.G., Evans, N.J., 2019. Sulfur isotopes, trace element, and textural analyses of pyrite, arsenopyrite and base metal sulfides associated with gold mineralization in the Pataz-Parcoy district, Peru: implication for paragenesis, fluid source, and gold deposition mechanisms. Miner Deposita. 54, 1077–1100.
Wang, J.B., Wang, Y.W., He, Z.J., 2006. Ore deposits as a guide to the tectonic evolution in the East Tianshan Mountains, NW China. Geol. China. 33, 461–469 (in Chinese with English abstract).
Wang, Y.H., Zhang, F.F., 2016. Petrogenesis of early Silurian intrusions in the Sanchakou area of Eastern Tianshan, Northwest China, and tectonic implications: geochronological, geochemical, and Hf isotopic evidence. Int. Geol. Rev. 58, 1294–1310.
Wang, Y., Zhang, F., 2018. Ore Genesis and hydrothermal evolution of the Donggebi Porphyry Mo Deposit, Xinjiang, Northwest China: evidence from isotopes (C, H, O, S, Pb), fluid inclusions, and molybdenite Re-Os dating. Econ. Geol. 113 (2), 463–488.
Webber, A.P., et al., 2017. The formation of gold-rich seafloor sulfide deposits: Evidence from the Beebe hydrothermal vent field, Cayman Trough. Geochem. Geophysi., Geosyst. 18 (6), 2011–2027.
Williams-Jones, A.E., Heinrich, C.A., 2005. Vapor transport of metals and the formation of magmatic-hydrothermal ore deposits. Econ. Geol. 100, 1287–1312.
Wilkinson, J.J., 2001. Fluid inclusions in hydrothermal ore deposits. Lithos 55, 229–272.
Windley, B.F., Alexeiev, D., Xiao, W., Kröner, A., Badarch, G., 2007. Tectonic models for accretion of the central Asian Orogenic Belt. J. Geol. Soc. London 164, 31–47.
Wu, Y.S., Wang, P., Yang, Y.F., Xiang, N., Li, N., Zhou, K.F., 2014. Ore geology and fluid inclusion study of the Donggebi giant porphyry Mo deposit, eastern Tianshan, NW China. Geol. J. 49, 559–573.
Xiao, W.J., Zhang, L.C., Qin, K.Z., Sun, S., Li, J.L., 2004. Paleozoic accretionary and collisional tectonics of the Eastern Tianshan (China): implications for the continental growth of Central Asia. Am. J. Sci. 304, 370–395.
Xiao, W.J., Windley, B.E., Allen, M.B., Han, C.M., 2013. Paleozoic multiple accretionary and collisional tectonics of the Chinese Tianshan orogenic collage. Gondwana Res. 23, 1316–1341.
Xiao, W.J., Sun, M., Santosh, M., 2015. Continental reconstruction and metallogeny of the circum-Junggar areas and termination of the southern central Asian Orogenic Belt. Geosci. Front. 6, 137–140.
XXMCL (Xinjiang Xituo MiningCo. Ltd), 2017. A Survey of Huangtan Gold and Copper Deposit in Hami City, Xinjiang. pp: 1–106.
Yu, M.J., Wang, Y.W., Wang, J.B., Mao, Q.G., Deng, X.H., Sun, Y., Zhang, R., 2019. The mineralization of the Kalatage arc, Eastern Tianshan, NW China: Insights from the geochronology of the Meiling Cu-Zn(-Au) deposit. Ore Geol. Rev. 107, 72–86.
Zang, W., Fyfe, W.S., 1995. Chloritization of the hydrothermally altered bedrock at the Igarapé Bahia gold deposit, Carajás, Brazil. Mineral. Deposita 30, 30–38.
Zartman, R.E., Doe, B.R., 1981. Plumbotectonics-the model. Tectonophysics 75, 135–162.
Zaw, K., Hunns, S.R., Large, R.R., Gemmell, J.B., Ryan, C.G., Mernagh, T.P., 2003. Microthermometry and chemical composition of fluid inclusions from the Mt. Chalmers volcanic-hosted massive sulfide deposit, central Queensland, Australia: implications for ore genesis. Chem. Geol. 194 (1–3), 225–244.
Zhang, L.C., Qin, K.Z., Xiao, W.J., 2008. Multiple mineralization events in the eastern Tianshan district, NW China: isotopic geochronology and geological significance. J. Asian Earth Sci. 32, 236–246.
Zhang, L.C., Shcn, Y.C., Ji, J.S., 2003. Characteristics and genesis of Kanggur gold deposit in the eastern Tianshan mountains. NW China: evidence from geology, isotope distribution and chronology. Ore Geol. Rev. 23, 71–90.
Zhang, Y.Y., Yuan, C., Long, X.P., Sun, M., Huang, Z.Y., Du, L., Wang, X.Y., 2017. Carboniferous bimodal volcanic rocks in the Eastern Tianshan, NW China: evidence for arc rifting. Gondwana Res. 43, 92–106.
Zhu, Z.Y., Cook, N.J., Yang, T., Ciobanu, C.L., Zhao, K.D., Jiang, S.Y., 2016. Mapping of sulfur isotopes and trace elements in sulfides by LA-(MC)-ICP-MS: potential analytical problems, improvements and implications. Minerals 110, 1–14.